POLYMER NANOCOMPOSITES: POLYMER AND PARTICLE DYNAMICS AND ITS APPLICATION AS LUBRICANT

A Thesis

Presented to the Faculty of the Graduate School

of Cornell University

In Partial Fulfillment of the Requirements for the Degree of

Master of Science

(Chemical Engineering)

by

Daniel June Kim

August 2012

ABSTRACT

My thesis is prepared upon two separate yet interdisciplinary projects. First, I present a project entitled 'Polymer Nanocomposites: Polymer and Particle Dynamics' where I investigate dynamics of polymer and particle upon their mixing. On second part of the thesis, I present one of the application of polymer nanocomposites (PNC) entitled 'Nanoscale Organic-Inorganic Hybrid Lubricants'. Understanding nanoscale dynamics of polymer and particle upon mixing will be a useful guide to improve its application.

Polymer Nanocomposites: Polymer and Particle Dynamics - Polymer nanocomposites containing nanoparticles smaller than the random coil size of their host polymer chains are known to exhibit unique properties, such as lower viscosity and glass transition temperature relative to the neat polymer melt. It has been hypothesized that these unusual properties result from fast diffusion of the nanostructures in the host polymer, which facilitates polymer chain relaxation by constraint release and other processes. In this study, the effects of addition of sterically stabilized inorganic nanoparticles to entangled cis–1,4–polyisoprene and polydimethylsiloxane on the overall rheology of nanocomposites are discussed. In addition, insights about the relaxation of the host polymer chains and transport properties of nanoparticles in entangled polymer nanocomposites are presented. The nanoparticles are found to act as effective plasticizers for their entangled linear hosts, and below a critical, chemistry and molecular–weight dependent particle volume fraction, lead to reduced viscosity, glass transition temperature, number of entanglements, and polymer relaxation time. We also find that the particle motions in the polymer host are hyperdiffusive and at the nanoparticle length scale, the polymer host acts like a simple, ideal fluid and the composites' viscosity rises with increasing particle concentration.

Nanoscale Organic-Inorganic Hybrid Lubricants - Silica (SiO_2) nanoparticles densely grafted with amphiphilic organic chains are used to create a family of organic-inorganic hybrid lubricants. Short sulfonate-functionalized alkylaryl chains covalently

tethered to the particles form a dense corona brush that stabilizes them against aggregation. When these hybrid particles are dispersed in poly-α-olefin (PAO) oligomers, they form homogeneous nanocomposite fluids at both low and high particle loadings. By varying the volume fraction of the SiO_2 nanostructures in the PAO nanocomposites, we show that exceptionally stable hybrid lubricants can be created and that their mechanical properties can be tuned to span the spectrum from simple liquids to complex gels. We further show that these hybrid lubricants simultaneously exhibit lower interfacial friction coefficients, enhanced wear and mechanical properties, and superior thermal stability in comparison with either PAO or its nanocomposites created at low nanoparticle loadings. Profilometry and energy dispersive X-ray spectroscopic analysis of the wear track show that the enhanced wear characteristics in PAO-SiO_2 composite lubricants originate from two sources: localization of the SiO_2 particles into the wear track and extension of the elastohydrodynamic lubrication regime to Sommerfeld numbers more than an order of magnitude larger than for PAO.

BIOGRAPHICAL SKETCH

Daniel Kim earned his Bachelor of Science degree in Chemical and Biomolecular Engineering from Cornell University in 2009. He received his Master of Engineering degree in Chemical and Biomolecular Engineering from Cornell University in 2010. He worked as a research assistant for Prof. Archer from August 2010 to May 2011. On June 2011 he joined the Master of Science program in Chemical and Biomolecular Engineering at Cornell University. On July 2012 he joined Doctor of Philosophy program in Chemical Engineering at University of Southern California.
While pursuing his degrees, Daniel Kim worked as a research assistant from distinctive research labs from the department of Chemical and Biomolecular Engineering at Cornell University. During summer 2008, he worked as a research assistant from Korea Institute of Energy and Research.

ACKNOWLEDGMENTS

I feel truly blessed to spend seven years of my life at Cornell University as I have found the true passion in my life and made good friends who have enriched my life. My experiences at Cornell allowed me to become self-inspired, productive, creative, adaptive and tough, all of which are crucial for success in graduate studies. Thus, I am confident that my experiences at Cornell will be a great asset as I embark on my new journey as a PhD student.

I would like to thank Prof. Lynden A. Archer who gave me the opportunity and support to be part of his research group. In his guidance, I learned what it takes to be a scientist. His diligence and passion in research worked as a guidance for me to survive through three years of post-baccalaureate research life at Cornell. Whenever I needed advice on both academics and life, he always made the time to provide thoughtful and insightful answers to me. I wouldn't have reached my dream if I didn't meet him.

Also, I would like to thank Prof. Yong L. Joo who happily agreed to support me as a committee member. His mentorship had tremendous impact on my life. Also, I learned responsibility and mindset I need to have to stay in academia and in the field of science. Also, I would like to thank Prof. Claude Cohen who gave me an opportunity to serve as a TA and was always encouraged me to find the true passion of my life.

I would also like to thank my family who was always supportive throughout my life. I wouldn't have survived without them. Also, I can't forget my dearest friends who were always there for me through both good and bad times. Lastly, I give my sincere thanks to Jesus Christ who filled my soul.

TABLE OF CONTENTS

LIST OF FIGURES

LIST OF TABLES

Chapter 1 Polymer Nanocomposites: Polymer and Particle Dynamics

1.1 Introduction

Polymer nanocomposites have attracted consistent research interest for the last few decades. This interest can be traced to the unique material properties such as tensile strength, hardness, refractive index, conductivity, etc. that can be achieved upon homogeneous dispersion of nanoscale fillers into a host polymer of practically any chemistry.[1–14] It is sustained by the broad range of potential applications in diverse fields - electrochemical energy storage, electronics, optics, lubricants, and photovoltaics, that would be enabled by controlled dispersion of nanoparticles in polymers.[1,2,4,7,12] Uniform dispersion of nanoparticles in polymer hosts is difficult for a variety of reasons, including their affinity towards aggregation owing to attractive van der Waals and polymer mediated depletion attraction forces.[9] A facile approach to mitigate the nanoparticle aggregation is through steric stabilization of the nanoparticles, wherein polymers are absorbed/grafted onto the particle surface, allowing stable dispersions of nanoparticled in versatile media ranging from simple liquids to elastic polymers.[4–8]

Recently, novel nanocomposites with the particle size being smaller than the random coil size (R_g) of the polymer but greater than both the tube diameter (a_T) and the correlation length (ξ) of the entangled polymer host were reported to exhibit enhanced nanoparticle stability.[10–14] Additionally, these uniform blends of entangled polymers and nanoparticles were also shown to exhibit unique properties including non–Einsteinian viscous properties, with lower viscosities found in the blends than in the host polymer, and a decrease in the glass transition temperature (T_g) of the nanocomposite. It has been suggested that the non–Einsteinian viscous properties reported in entangled-polymer nanoparticle composites arise from the ability of the diffusing particles to release entanglement constraints between the host polymer.[10–12] However, the absence of in–depth investigations of these phenomena, including the

effects of nanoparticles on various relaxation processes associated with these systems, has prevented generalization of these ideas.

Herein, we investigate nanocomposites comprised of silica (SiO_2) nanoparticles functionalized with tethered polymer chains and suspended in highly entangled polymer chains with similar chemistry as the tethered polymers. A variety of systems are considered with the tethered/host polymer combinations including cis–1,4–polybutadiene (PBD)/cis–1,4–polyisoprene (PI), cis–1,4–polyisoprene (PI)/cis–1,4–polyisoprene (PI) and polydimethylsiloxane (PDMS)/polydimethylsiloxane (PDMS). A range of experimental techniques including mechanical rheology, differential scanning calorimetry (DSC), broadband dielectric spectroscopy (BDS), and X–ray photon correlation spectroscopy (XPCS) are utilized to characterize the effect of the particles on dynamics of their polymer host, and vice versa, in these nanocomposites. We focus particularly on the SiO_2–PBD/PI nanocomposites for the following reasons: first, PI is a type–A dielectric material[15–17], implying that the polymer has a net dipole moment parallel to its end–to–end vector; PBD in contrast is dielectrically inert. Broadband Dielectric Spectroscopy of these nanocomposites can therefore be used to selectively probe the chain–scale relaxation dynamics of the PI host polymer as influenced by the addition of nanoparticles.[17] Second, the close to zero interaction parameter for a PBD/PI mixture implies negligible enthalpic interaction between the tethered and host polymer.[18] Lastly, higher electron density of the silica core than that of the tethered as well as host polymer allows for facile characterization of the nanoparticle motion through X–ray photon correlation spectroscopy.

1.2 Nanocomposites: Synthesis and Characterization

Nanocomposites with precise SiO_2 contents were prepared by mixing tethered SiO_2 nanoparticles with the host polymer. The SiO_2–PBD nanoparticles were synthesized by following a two–step reaction scheme. In the first step, 10 nm SiO_2 nanoparticles (Ludox^{TM} SM–30, supplied by Sigma Aldrich) were functionalized with sulfonic acid using previously reported procedure.[5,7,19,20] Briefly, an excess of 3–(trihydroxysilyl)–

1–propanesulfonic acid (supplied by Gelest Inc.) was added drop–wise at 70℃ to a dilute suspension of the SiO_2 particles in DI water with rapid stirring and the mixture was incubated over night at pH 2. Untethered sulfonic acid molecules were subsequently removed via repeated dialysis of the reaction mixture against DI water and the sodium ions on the particles were removed through ion exchange reactions. The acid functionality of the nanoparticles was determined by titration against standard sodium hydroxide solution.

In the second step, amine–functionalized cis–1,4–polybutadiene (PBD) chains (Mw = 3 KDa, Mw/Mn ~ 1.05 and Rg ~ 1.79 nm, supplied by Polymer Source Inc.) were dissolved in tetrahydrofuran (THF) and a stoichiometric amount of sulfonic acid functionalized SiO_2 nanoparticles in DI water was added drop–wise to the solution. The reaction was allowed to proceed over several days to ensure maximal grafting of the chains and the excess PBD chains were then removed by repeated precipitation in a methanol/THF mixture. Finally, the solvents were removed by vacuum drying and the SiO_2 content in the resulting SiO_2–PBD nanoparticles was found to be 11 wt%, as determined by thermogravimetric analysis (TGA) of the nanoparticles (TA Instruments TGA Q500), from which the grafting density (Σ) of the PBD chains was estimated to be 1.9 chains/nm^2. Figure 1a shows a transmission electron micrograph of these SiO_2–PBD particles and it is evident that nanoparticle cores are very well dispersed even in the absence of any suspending medium. Tethered nanoparticles with such high grafting densities have been shown to be stable against aggregation and exhibit fluid like properties.[5,15,16] The strain–dependent rheology of these SiO_2–PBD nanoparticle, as shown in Figure 1b, illustrates the soft-glassy behavior of these nanoparticle fluids and further validates the absence of any aggregation in these systems.[5,7,15,16] Further, the low–strain elastic modulus of these nanoparticle fluids is comparable with that of the entangled PI host (not shown here).

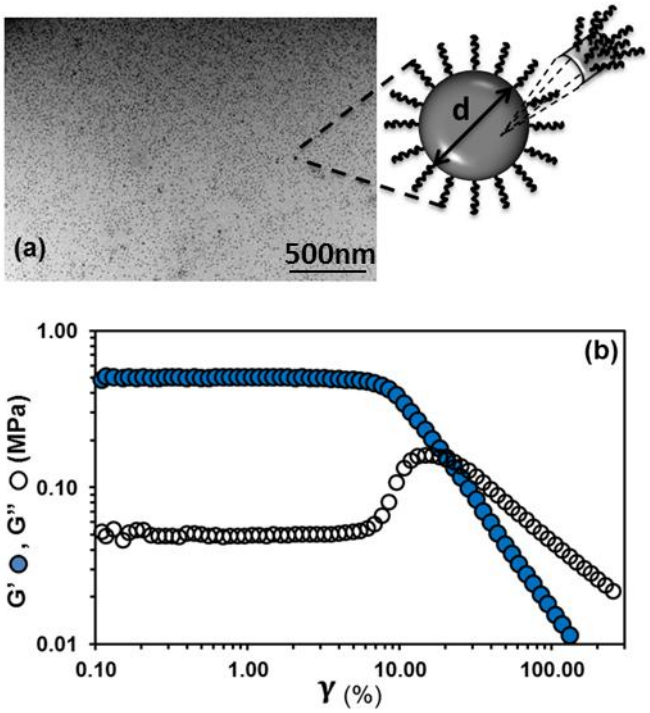

Figure 1: (a) Transmission electron micrograph and **(b)** Strain-dependent storage, *G',* and loss *G''* moduli for of SiO_2–PBD nanoparticles at a fixed oscillation frequency $\omega = 10\ s^{-1}$ and T = 30°C.

SiO_2–PBD/PI nanocomposites were prepared by mixing the suspensions of the SiO_2–PBD nanoparticles in chloroform with cis–1,4–polyisoprene (PI) (M_w = 316 KDa, M_w/M_n ~ 1.27, R_g ~ 18.39 nm, supplied by Polymer Source Inc). Chloroform was subsequently removed by vacuum drying to obtain the nanocomposite samples. By adjusting the relative proportion of the two components, nanocomposites with SiO2 contents ranging from 0.5 wt% to 5.5 wt% were synthesized. Similar procedures were employed to synthesize SiO_2–PI/PI (Σ ~ 2.8 chains /nm^2) and SiO_2–PDMS/PDMS (Σ ~ 1.1 chains /nm^2) nanocomposites with variable nanoparticle contents.

1.3 Mechanical Rheology

The effect of nanoparticles on the host polymer viscosity were characterized through steady–shear measurements performed at shear rates performed at shear rates ($\dot{\gamma}$) in the range $5\times10–4\ s^{-1} \leq \dot{\gamma} \leq 5\times10–2\ s^{-1}$. These measurements were carried out at 30℃

using a Rheometrics ARES rheometer outfitted with 10 mm diameter parallel plate fixtures and were repeated multiple times to obtain better statistics. A Newtonian plateau at low shear rates is observed for all the SiO_2–PBD/PI nanocomposites, as shown in Figure 2a, which ultimately gives way to shear thinning behavior at high rates. Further, in agreement with recent studies[10–14], Figure 2a clearly shows that the viscosity η of the SiO_2PBD/PI (3K–PBD/316K–PI) nanocomposites decreases as the particle content increases. Figure 3a shows that the relative zero–shear viscosity η_r ($\equiv \eta_{0,NC}/\ \eta_{0,P}$) of the SiO_2PBD/PI nanocomposites (NC) are not only lower than 1 but also decreases as the SiO2 core volume fraction (ϕ) rises. This behavior is in complete contrast to the classical predictions by Einstein's[21] and Batchelor's[22], where the relative viscosity of a suspension of particles is predicted to rise at least linearly with the volume fraction of suspended particles.

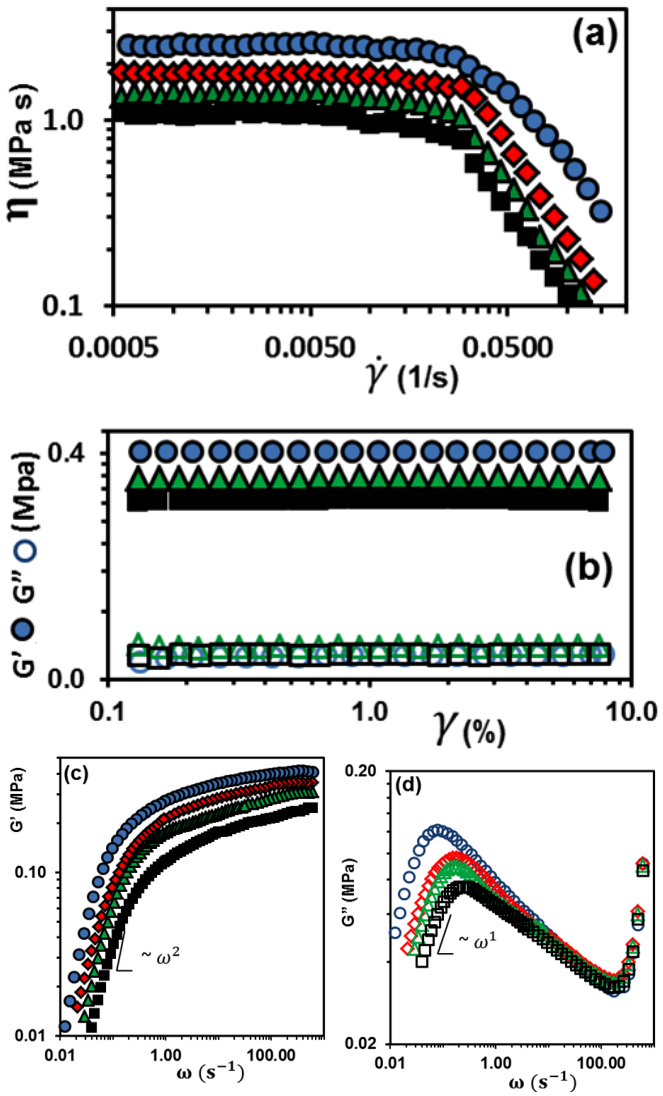

Figure 2: (a) Viscosity versus shear rate, **(b)** Storage modulus, *G'*, and loss modulus, *G"* versus strain amplitude γ, **(c)** *G'* vs. oscillation frequency ω and **(d)** *G"* vs. ω for SiO_2–PBD/PI nanocomposites. Different symbols denote various particle loadings – circle: ϕ = 1%, triangle: ϕ = 3%, and square: ϕ = 5%.

Figure 3b shows results for various other nanocomposites, all of which show similar non–Einsteinian initial depression of the host polymer's viscosity upon addition of nanoparticles. For comparison, η_r vs. ϕ trends for a SiO_2–0.9KPDMS/0.95KPDMS nanocomposite are also included in the figure. For this case, the host polymer is unentangled and its random–coil size (R_g ~ 0.77 nm) is substantially lower than the radius of the SiO_2 nanoparticle cores. This material exhibits a relative viscosity that rises in proportion to the ϕ, consistent with expectations for a suspension of particles.

Also, unlike the SiO_2–PBD/PI nanocomposite, for which η_r decreases continuously with ϕ in the range studied, all of the other materials show an initial decrease at low ϕ which is followed by a more conventional suspension regime in which ηr increases with ϕ. Further inspection of the results indicate that the nanoparticle composition range where the non–Einsteinian behavior is observed shrinks as the molecular weight of the polymer host is reduced and as the effective hardness (SiO_2 particle size/corona thickness) of the nanoparticles becomes greater.

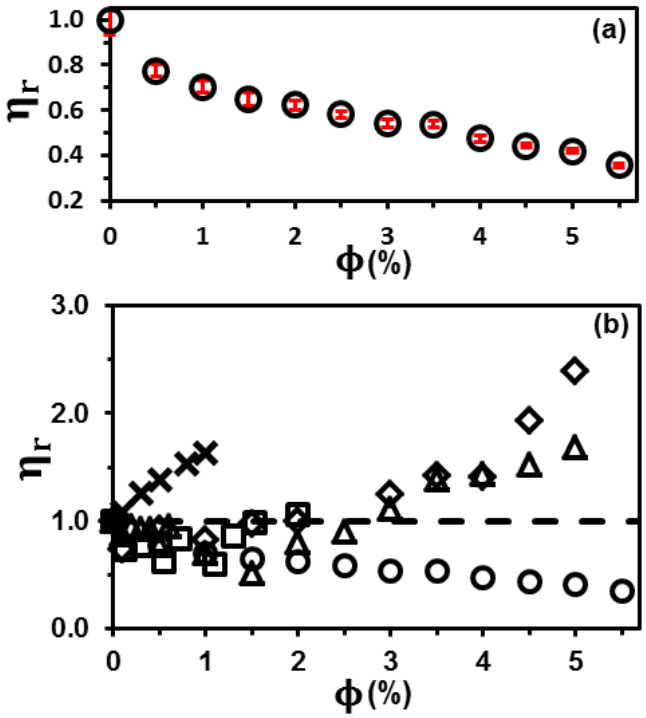

Figure 3: Plot of η_r vs. ϕ for (nanoparticle type/suspending medium): **(a)** SiO_2–3KPBD/316KPI; **(b)** ×: SiO_2–0.9KPDMS/0.95KPDMS; squares: SiO_2–0.5KPI/304KPI; diamonds: SiO_2–C12/304KPI3; triangles: SiO_2–0.9KPDMS/308KPDMS; circles: SiO_2–3KPBD/316KPI.

Strain dependent oscillatory shear measurements at a fixed oscillation frequency ω = 10 s^{-1} and over a broad range of shear strains (γ) were also performed on the SiO_2–PBD/PI nanocomposite using an Anton Paar MCR 301 rheometer, as shown in Figure 2b. In conjunction to the non–Einsteinian viscosity decrease in η, we also observe a significant decrease in the zero– and finite–strain rubbery plateau modulus, $G_{e,0}$ (≡

$G'_{\gamma\to 0}$) with increasing ϕ. We would like to specifically point out that these observations are in contrast to previous reports on non-Einsteinan trends in viscosity, where negligible changes in G' were reported.[10,11,13] These measurements were complemented by frequency–dependent oscillatory shear measurements at low shear strain ($\gamma = 0.01$) to obtain the limiting linear viscoelastic properties for the nanocomposites (Figs 2c & 2d). It is noteworthy from Figure 2d that the loss maximum progressively becomes more depressed and drifts to higher frequency with increasing ϕ. Together, these observations suggest that the addition of nanoparticles disrupts / dilates the polymer network and increases the effective entanglement molecular weight Me ($= \rho RT/G_{e,0}$), as depicted in Figure 4a.

1.4 Nanoparticle Effects on Glass Transition

Further insights into the influence of nanoparticles on the entanglement structure of their host was obtained from glass transition temperature (T_g) trends, estimated from Differential Scanning Calorimetry (DSC) (see Figure 5). These measurements were carried out at a fixed temperature ramp rate of 5 K/min in a nitrogen environment using a TA Instruments DSC Q2000. As illustrated in Figure 4b, the T_g of nanocomposite decreases progressively with increasing amount of SiO_2–PBD nanoparticle concentration. The T_g for a polymer blend can be estimated using the Fox relation,[23] $1/T_g = \Sigma_i\, m_i/T_{g,i}$, where mi and $T_{g,i}$ are mass fraction and T_g of each of the blend components. The dashed line in the figure is Fox relation estimate under the assumption that all of PBD chains tethered to the particles participate in plasticization of the host polymers. Clearly, the theoretical estimate yields a much larger T_g decrease than what is observed in the experiments. This leads us to believe that only a fraction of the PBD chain segments (presumably those near the unattached ends) participate in plasticization of the PI host and are responsible for the majority of the observed effects.

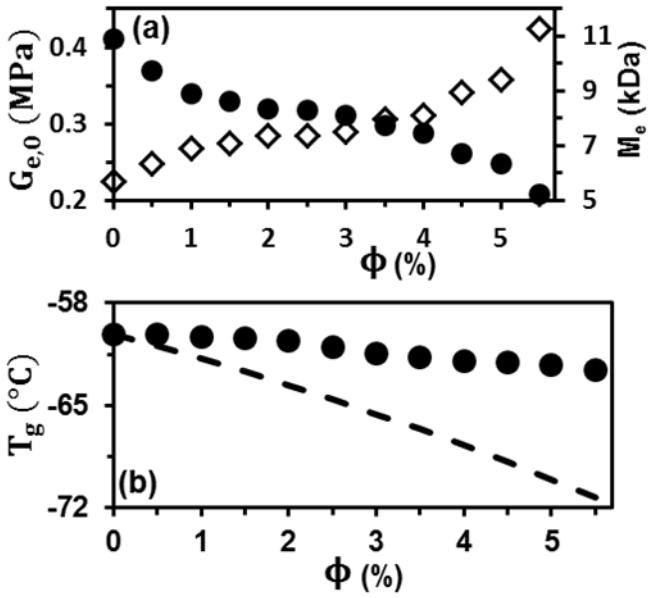

Figure 4 (a): Plateau modulus ($G_{e,0}$) and corresponding M_e vs. ϕ (closed and open symbol, respectively) and **(b)** T_g vs. ϕ for SiO_2–PBD/PI nanocomposites. The dotted line in (b) is prediction from Fox relation.

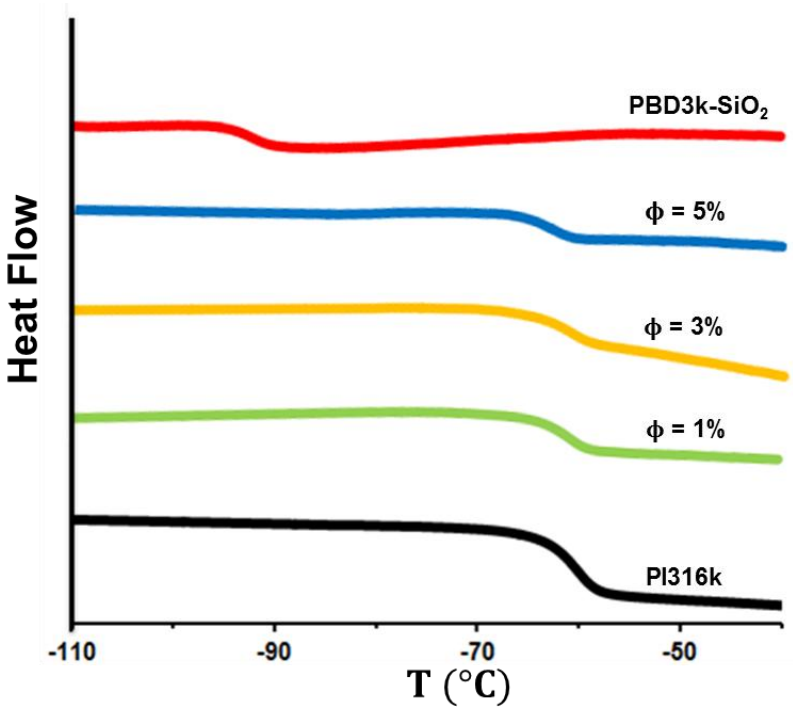

Figure 5: DSC thermograms of SiO_2–PBD nanocomposites for PI316k, ϕ = 1%, ϕ = 3%, ϕ = 5%, and PBD3k-SiO_2. Curves are shifted along vertical axis to enhance clarity.

An alternate way to quantify the extent of plasticization in these systems is through the normalized entanglement molecular weight, M_e/M_{e0}, which is calculated from plateau modulus as $M_e/M_{e0} = \rho RT/M_{e0}G_{e,0}(\phi)$. Here M_{e0} is the entanglement molecular weight of the host PI. M_e/M_{e0} is shown in Figure 6 to increase with increasing ϕ (diamonds), indicating progressive disentanglement of the host PI. Me/Me0 is also compared to theoretical estimates of the normalized entanglement molecular weight, which can be computed as $M_e/M_{e0} = \varphi^{-4/3}$, φ being effective PBD volume fraction (φ) participating in plasticization of the PI host. The two situations presented in Figure 6 correspond to the cases where φ is computed assuming (i) all PBD chains tethered to the nanoparticles are involved in plasticizing the host PI (circles); and (ii) only a fraction of the tethered PBD chains, computed from applying the Fox relation to the experimental T_g data (squares). It is evident from Figure 6 that although scenario (ii) is in better accord with the estimates from rheology measurements, although the agreement is quite far from being quantitative.

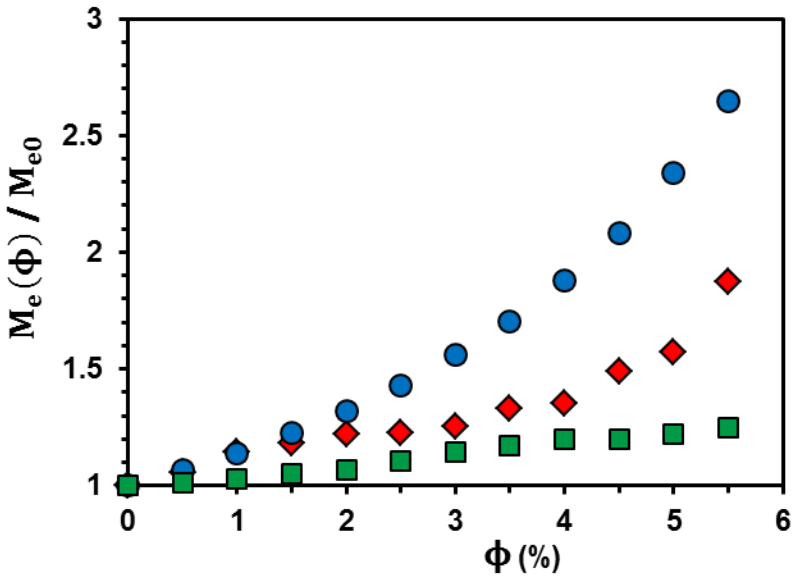

Figure 6: Normalized entanglement molecular weight, $M_e(\varphi)/M_{e0}$ vs. ϕ for SiO_2–PBD nanocomposites obtained from oscillatory amplitude sweep measurement (diamonds). Also, $M_e(\varphi)/M_{e0}$ estimates assuming (i) all PBD chains act as plasticizer (circles) and (ii) an effective amount of PBD calculated from T_g measurement act as plasticizer (squares). M_{e0} is the entanglement molecular weight for pure PI.

1.5 Broadband Dielectric Spectroscopy and Host Polymer Relaxation Dynamics

The novelty of the nanocomposites considered in this study lies in our ability to probe at the normal mode or end–to–end vector relaxation time of host chains systematically as influenced by the addition of the nanoparticles. Normal mode relaxation time (τ_p) of the host PI chains was characterized using a Novocontrol broadband dielectric spectrometer outfitted with sandwich–type gold–plated copper measurement fixtures. Dielectric loss spectra in the frequency range of 10^{-2} to 10^{7} Hz at temperatures ranging from – 60℃ to 130℃ were obtained using a quartz cryosystem with a nitrogen gas stream. Figure 5 reports the terminal relaxation time ($\tau_p \approx (2\pi f_p)^{-1}$) of PI chains with increasing loading of SiO_2–PBD nanoparticles, as estimated from the low frequency (f_p) maximum in the dielectric loss spectra (Figure 7). Clearly, τ_p of the PI host decreases markedly upon addition of nanoparticles at all temperatures, indicating a speeding up of chain relaxation upon nanoparticle addition. Also, τ_p is found to be a strong function of temperature.

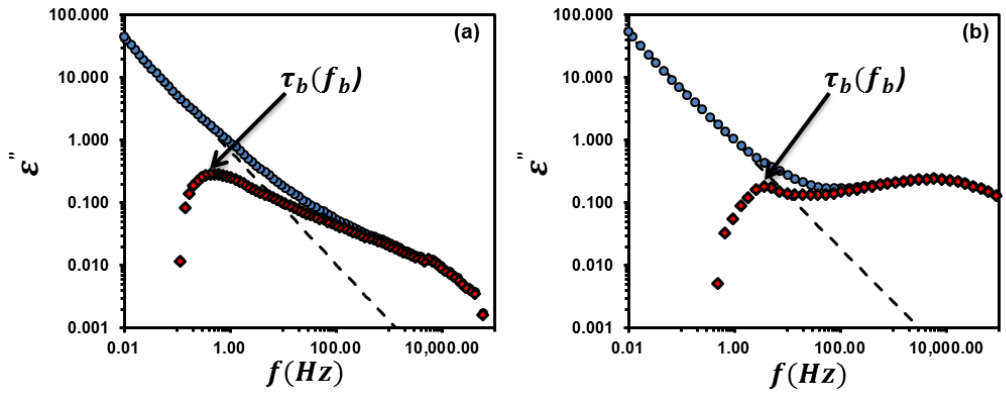

Figure 7: $\varepsilon''(f) = \varepsilon_d''(f) + \varepsilon_c''(f)$ calculation for (a) PI316k and (b) ϕ = 5% SiO_2–PBD nanocomposites. Circle symbol represents $\varepsilon''(f)$, dotted line represents $\varepsilon_c''(f)$ drawn from low frequency, and diamond symbol represents $\varepsilon_d''(f)$ which was used to find $\tau_p = (2\pi f_p)^{-1}$ where f_p corresponds to maximum in the dielectric loss spectrum, $\varepsilon_d''(f)$.

Further insights into the chain relaxation processes are obtained by fitting the relaxation data with the Vogel–Fulcher–Tamman (VFT) equation[24],

$$\ln(\tau) = A + \left(\frac{B}{T - C}\right) \qquad \text{(eq. 1)}$$

as shown with dashed lines in Figure 8. Here A is the high temperature limit of the relaxation time, B is the activation energy, T is the absolute temperature and C is the Vogel temperature. Values of these fitting parameters are summarized in Table 1. Both A and B decrease as the nanoparticle loading is increased, but the Vogel temperature (C) changes very little upon addition of nanoparticles to the host polymer. The Doolittle equation,[18] $\eta \sim \exp(B/f)$, provides a conventional approach for relating the viscosity (η) to the activation energy (B) and free volume (f) of a material; $f \propto (T - C)$. The fact that C is essentially unaffected by particle loading implies that the effect of the nanoparticles on T_g is not likely a result of an increased free volume due to the presence of nanoparticles or to the large numbers of ends introduced by the nanoparticle–tethered PBD chains.[25] Rather, the particles appear to reduce the activation barrier, B, for motion of the host, which for an entangled polymer manifests as a reduction of the number of entanglements, N_e ($= M_w/M_e$) per chain, consistent with our earlier conclusion from the $G_{e,0}$ data. Again, Mw is the molar mass of the PI host and M_e is the entanglement molecular weight computed from $G_{e,0}$. Further, as shown in the inset of Figure 8, τ_p is found to scale as $N_e^{3.4}$, as is expected for long entangled chains.[18] This provides a direct connection between the rheology data and relaxation experiments, and further confirms our hypothesis that addition of nanoparticles leads to dilation of the entanglement network and speeds up chain relaxation, which is in turn responsible for the lower viscosity of the nanocomposites as compared to the polymer host.

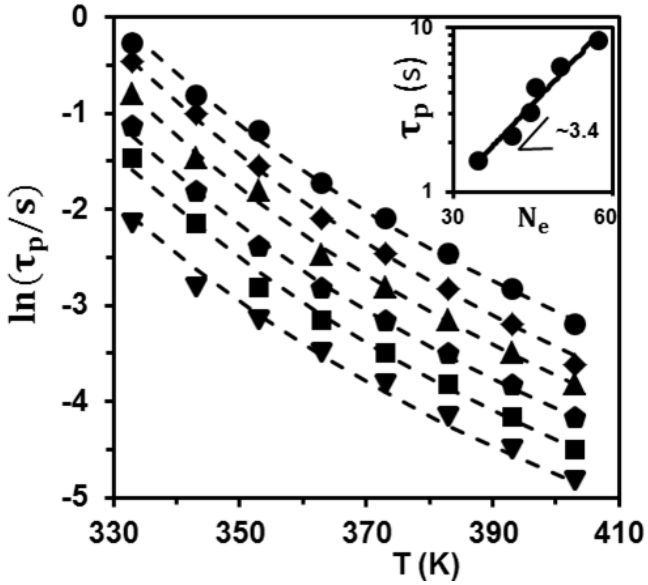

Figure 8: Temperature dependence of PI relaxation time (τ_p) for SiO_2–PBD/PI nanocomposites at various ϕ (circle: ϕ = 0, PI316k, diamond: ϕ = 1%, triangle: ϕ = 2%, pentagon: ϕ = 3%, square: ϕ = 4%, and inverted triangle: ϕ = 5%). Dotted lines are VFT fits to the data. Upper inset is a log-log plot of τ_p vs. N_e at 30^o C extrapolated using VFT fits.

ϕ(%)	A	B	C
0	-9.7	1466.5	179
1	-10.1	1460.0	182
2	-10.3	1430.2	182
3	-10.5	1395.4	181
4	-10.75	1384.1	182
5	-10.81	1320.0	181

Table 1: VFT fit parameters for SiO_2–PBD/PI nanocomposites.

1.6 X–ray Photon Correlation Spectroscopy and Nanoparticle Motion

In closing, we briefly consider the motions of the SiO_2 particles in the host polymer and the role they play in the phenomena discussed above. Relaxation processes associated with the nanoparticles are investigated using X–ray photon correlation spectroscopy (XPCS), where the temporal evolution of the X–ray scattering patterns from the nanocomposites reveal information about the dynamics of the silica core of the nanoparticles. XPCS measurements were performed at Sector 8–ID at the Advanced Photon Source (APS) across a range of the wave vector (q) using 7.35 keV

X–rays. Instrumental specifications can be found elsewhere.26 The normalized intensity–intensity autocorrelation function ($g_2(q,t)$), obtained from XPCS measurements, is related to the intermediate scattering function (ISF, f (q, t))[26] as

$$g_2(q,t) = 1 + b\,[f(q,t)]^2 \qquad \text{(eq.2)}$$

Here, b and t are the instrument dependent Siegert factor (~ 0.4), and the delay time respectively. Numerous studies26–28 have reported that the ISF, and consequentially g2(q,t), are best described by a stretched/compressed exponential functions of the form

$$f(q\,t) = \exp\,[-(t/\tau_n)^{\beta}] \qquad \text{(eq.3)}$$

with τ_n and β denoting the q dependent characteristic relaxation time and the stretching/compression exponent of the ISF. The bottom inset in Figure 6a shows typical g2(q, t) at q = 0.09 nm–1 for a nanocomposite with ϕ = 1%. The g2(q,t) results shown here, as well as for other nanocomposites, were fitted with the functional forms described by Eq. (2) and (3), and is shown as the solid line in the inset. β was found to vary between 1.5 and 2 with q for all the systems with no specific trends, indicating a compressed exponential relaxation and signifying a comparatively faster decay of the f(q t). Such a compression of the relaxation is commonly seen for nanoparticle motion in glassy media and has been attributed to the non-equilibrium forces present in the glassy, non-ergodic systems.27,28 As shown in Figure 9a, τ_n follows a decidedly q–1 scaling for all the nanocomposites studied, indicating that the nanoparticle cores are hyperdiffusive in the entangled polymer host. Similar observations have been reported in many other systems ranging from thin films to suspensions, where the nanoparticle diffusion is restricted due to an entangled host or jamming.26–30 We believe that such hyperdiffusive motion of the nanoparticles cores arises from their hopping between the cages formed by the entangled polymer around them. Additionally, as illustrated in the top inset for Figure 9a, at any q, τn increases with nanoparticle loading.

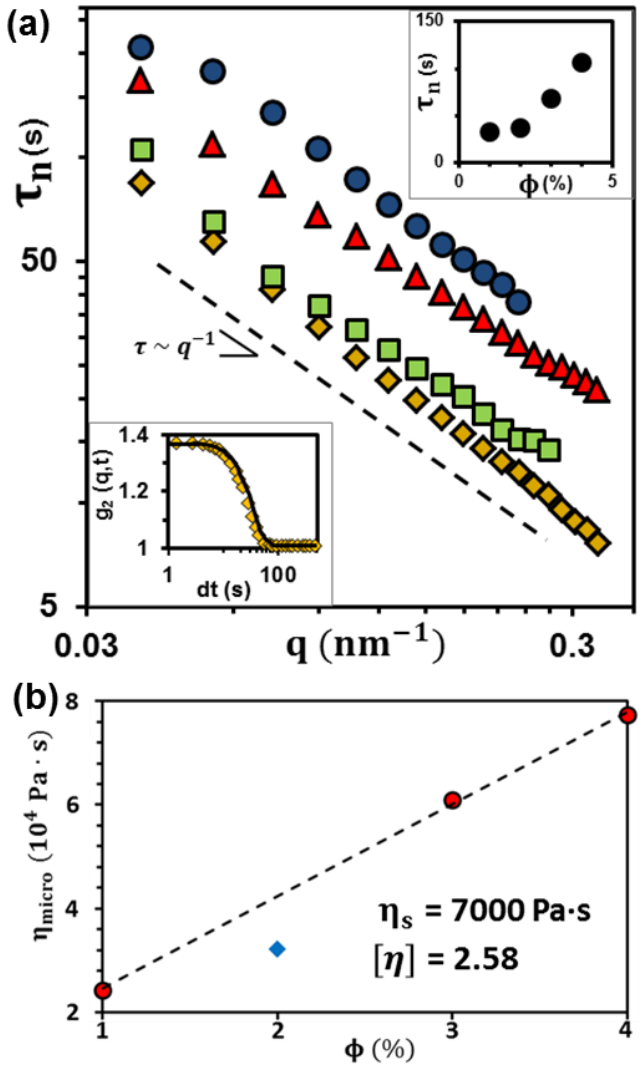

Figure 9: (a) τ_n vs. q for SiO_2–PBD/PI nanocomposites at various ϕ (diamond: ϕ = 1%, square: ϕ = 2%, triangle: ϕ = 3%, and circle: ϕ = 4%). Lower inset: g_2 vs. dt at q = 0.09 nm^{-1} for the ϕ = 1% nanocomposite. Upper inset: τ_n vs. ϕ at q = 0.09 nm^{-1}. **(b)** η_{micro} vs. ϕ for SiO_2–PBD/PI nanocomposites. Dotted line is a fit of the form $\eta = \eta_s(1 + [\eta]\phi)$ for 3 data points shown as circles only.

Balancing the viscous resistance on a hyperdiffusive nanoparticle with the Brownian force (kT/a) it experiences by collisions with surrounding molecules, $6\pi\eta_{micro}va = kT/a$, it is possible to estimate the effective/micro viscosity (ηmicro) the nanoparticles experience in the host polymer. Here v (= $q\tau_n$) is the average particle velocity determined from the XPCS measurement,[27] a is the particle radius and k is the Boltzmann constant. Surprisingly, in contrast to bulk viscosity (η), η_{micro} is found to be a linearly increasing function of particle volume fraction with a slope of 2.58 (Figure

9b), which is very close to Einstein's result21 for intrinsic viscosity η (= 2.5) of hard spheres.

ϕ(%)	N_e	a_T (nm)	v (nm/s)	η_{micro} (MPa s)	η (MPa s)
1	45.8	5.7	0.36	0.02	1.79
2	43.0	5.5	0.28	0.03	1.59
3	42.0	5.4	0.15	0.06	1.38
4	38.9	5.2	0.11	0.08	1.22

Table 2: Number of entanglement per chain (N_e), tube diameter (a_T), drift velocity of particle (v), microscopic viscosity (η_{micro}) and bulk viscosity (η) for SiO_2–PBD/PI nanocomposites.

A competition between two effects with increasing ϕ where increasing nanoparticle crowding hinders an individual nanoparticle motion while the fraction of tethered chains participating in the plasticization of the polymer host progressively decreases can be attributed to explain the opposing trends in η_{micro} and η. While the former dominates ηmicro even at the lowest particle loading considered, its effects on η are much less dramatic. However, we expect the particle crowding effects to eventually supersede the plasticization effects from the PBD chains and lead to an upturn in the bulk viscosity as well, as is observed for nanocomposites with particles having smaller corona (Figure 1b).

1.7 Conclusion

In conclusion, we have discovered that nanoparticles with densely grafted polymer chains act as effective plasticizers when suspended in well-entangled polymer hosts. The level of plasticization is a weak function of the nanoparticle volume fraction, which is interpreted to mean that only a fraction of each grafted polymer chain participates in producing the effect. Both the number of entanglements per host chain and the glass transition temperature of the host polymer are found to decrease upon particle addition. Further, the end-to-end vector relaxation time of the host chains is found to decrease in a manner consistent with theoretical estimates for solvent-dilation of the entangled polymer network. Characterization of the microscopic motion of the

particles in the host reveals that nanoparticle motions in entangled polymers are hyperdiffusive, but that the migrating particles experience their environment as a local viscosity, substantially smaller than the bulk viscosity of the host polymer, which increases proportionately with the volume fraction of particles in the nanocomposites. As a first step towards connecting the strikingly different influences of nanoparticles on the macro– and microscopic viscosity in these composites, we contend that they stem from a balance between two principal effects. First, increasing the loading of sterically stabilized nanoparticles in the composites increases the tethered corona content, which plasticizes the host polymer, increases its entanglement spacing, and lowers the viscosity, chain relaxation time, and plateau modulus. In contrast, increasing the particle content in the composites enhances crowding, which inhibits particle motion and causes progressive increase in the particle relaxation time.

References

1. A. C. Balazs, T. Emrick and T. P. Russell, Science, 2006, 314, 1107.
2. D. R. Paul and L. M. Robeson, Polymer, 2008, 49, 3187.
3. Q. Zhang and L. A. Archer, Langmuir, 2002, 18, 10435.
4. P. Akcora et. al., Nat. Mater., 2009, 8, 354.
5. P. Agarwal, H. Qi and L.A. Archer, Nano Lett. , 2010, 10, 111; P. Agarwal and L. A. Archer, Phys. Rev. E, 2011, 83, 041402.
6. C. Chevingny et. al., Macromolecules, 2011, 44, 122.
7. S. Srivastava, P. Agarwal and L.A. Archer, Langmuir, 2012, 28, 6276.
8. S. Srivastava, J. H. Shin and L.A. Archer, Soft Matter, 2012, 8, 4097.
9. W. B. Russel, D. A. Saville and W. R. Schowalter, Colloidal Dispersions, Cambridge University Press, Cambridge, 1989.
10. M. E. Mackay, T. T. Dao, A. Tuteja, D. L. Ho, B. V. Horn, H. Kim and C. Hawker, Nat. Mater. 2003, 762, 31872
11. A. Tuteja, M. E. Mackay, C. J. Hawker and B. van Horne, Macromolecules 2005, 38, 8000

12. M. E. Mackay, A. Tuteja, P. M. Duxbury, C. J. Hawker, B. V. Horn, Z. Guan, G. Chen and R. S. Krishnan, Science 2006, 311, 1740.
13. K. Nusser, G. J. Schneider, W. Pyckhout–Hintzen and D. Richter, Macromolecules 2011, 44, 7820.
14. R. G. Schmidt, G. V. Gordon, C. A. Dreiss, T. Cosgrove, V. J. Krukonis, K. Williams and P. M. Wetmore, Macromolecules 2010, 43, 10143.
15. M. E. Baur and W. H. Stockmayer, J. Chem. Phys. 1965, 43, 4319.
16. H. Watanabe, Macromol. Rapid. Comm. 2001, 22, 127.
17. P. Agarwal, S. Kim and L. A. Archer, submitted (2012).
18. M. Rubinstein and R. H. Colby, Polymer Physics; Oxford University Press: New York, 2003.
19. R. Rodriguez, R. Herrera, L. A. Archer and E. P. Gianellis, Adv. Mater. 2008, 20, 4353.
20. D. Kim and L. A. Archer, Langmuir. 2011, 27, 3083.
21. A. Einstein, Ann Phys. 1906, 19, 317.
22. G. K. Batchelor et. al., J. Fluid Mech., 1977, 35, 97.
23. P. R. Couchman, Phys. Lett. A, 1979, 70, 155.
24. C. A. Angell, K. L Ngai, G. B. Mckenna, P. F. Mcmillan and S. W. Martin, J. Appl. Phys., 2000, 88, 3113.
25. P. G. Santangelo, C. M. Roland, K. L. Ngai, A. K. Rizos and H. Katerinopoulos, J. Non–Cryst. Solids., 1994, 172, 1084.
26. R. L. Leheny, Curr. Opin. Colloid Interface Sci., 2012, 17, 3.
27. S. Narayaran, D. R. Lee, A. Hagman, X. Li and J. Wang, Phys. Rev. Lett. 2007, 98, 185506.
28. H. Guo et. al., Phys. Rev. Lett., 2009, 102, 075702.
29. L. Cipelletti et. al., Phys. Rev. Lett., 2000, 84, 2275.
30. L. Cipelletti et. al., Faraday Discuss., 2003, 123, 237.

Chapter 2 Nanoscale Organic-Inorganic Hybrid Lubricants

2.1 Introduction

Historically, a wide variety of lubricating materials have been used to reduce interfacial friction and enhance wear-resistance of surfaces. The lubricant is believed to perform these functions by forming a stable interfacial film between two proximate surfaces, thereby increasing their load carrying capacities and reducing friction. The degree to which any lubricant reduces wear depends on a variety of factors, including interface chemistry, surface roughness, sliding speed, normal load, contact geometry, and tribo-mechanical/chemical characteristic of the lubricating film[1-6]. In the last decade, there has been growing interest in developing so-called *hybrid lubricants* in which various types of inorganic nanoparticles are incorporated as additives in base lubricating oils[7-20]. To facilitate satisfactory dispersion of the nanoparticles, dispersants[7-14] or surface modifying agents[15-22] are typically employed. Significantly, all of these studies show that even a small amount of nanoparticles added in the base oil yields measurable reductions in the interfacial friction coefficient and improvements in anti-wear properties of the lubricant.

A popular hypothesis in the field is that nanoparticle additives enhance the interfacial friction and wear properties of a lubricant by creating mechanically strong, homogeneous (no aggregates) load bearing films, which reduce surface-to-surface contact. The improvements in friction and anti-wear properties have also been contended to arise from deposition of reinforcing hard nanoparticles into the wear track[19-22]. All of these benefits should improve, at least in principle, as the nanoparticle loading is increased. In practice, however, aggregation and/or phase separation of the nanoparticles makes it difficult to maintain stable dispersion at high particle loadings[7-22], which defeats the benefits of adding nanoparticles to the base oil; this effect manifests both as a loss of transparency of the hybrid lubricant and as a gradual worsening of its mechanical properties. In addition to facile deposition of densely dispersed nanoparticles into the wear track, particles are also expected to impart

desirable temperature stability in the lubricant's viscous properties[7]. In particular, because significant changes in the lubricant's viscosity upon increase in temperature alters the thickness, structure and stability of the lubricating film between rubbing surfaces, its effect on wear might mitigate any positive benefits produced by deposition of nanoparticles. Similar insensitivity of viscosity on sliding speed would also seem desirable, but this effect has been investigated in less detail.

Herein we report on synthesis and tribological behaviors of a family of PAO-based organic-inorganic hybrid lubricants created by dispersing densely functionalized nanoscale organic hybrids (NOHMs[23-24] and NIMs[25-27]) in PAO oligomers. Significantly, the hybrid lubricants manifest exceptionally stable interfacial friction and wear properties at high nanoparticle loadings. Although demonstrated here using PAO base oils, nanoscale hybrid lubricants created using other lubricating fluids are possible using NOHMs or NIMs to facilitate complete integration of sticky metal oxide nanoparticles into the lubricant media at high particle loadings. For example, work underway in the group shows that very similar material properties to those reported in this article are achieved in NOHMs/Polydimethylsiloxane (PDMS) hybrid lubricants. Our group has previously found that PDMS based thin-film lubricant covalently tethered to the self-assembled monolayer (SAM) provides exceptional reductions in friction coefficient[28-29]. An additional attractive feature expected from our hybrid lubricants is that interactions between the substrates to be lubricated and the reinforcing nanoparticles can be tuned through the chemistry of the corona chains. For example, nanoscale hybrid particles comprised of organic amine corona are known to interact strongly with metallic substrates even at elevated temperature, which should enhance both the stability and high-temperature wear characteristics of hybrid lubricants employing these particles.

2.2. Experimental Section

2.2.a. Preparation of PAO-NOHMs composite lubricants

Nanoscale organic hybrid materials were synthesized by tethering a base-stabilized organic silane to SiO_2 nanoparticles suspended in H_2O, a 40 wt%, NaOH stabilized aqueous suspension of 12 nm diameter SiO_2 in water, was purchased from Sigma-Aldrich Chemicals and used as received. (3-Trimethoxysilylpropyl)-Diethylenetriamine (TMS-PDTA) was purchased from Gelest, Inc. and used to form corona around the SiO_2 core (as shown in Fig. 1A). Prior to the linking reaction, the LUDOX suspension was diluted in DI water to form a 3 wt% solution. TMS-PDTA in large excess (2g TMS-PDTA: 1 g SiO_2) was divided into three aliquots and added drop-by-drop to the silica dispersion maintained at a temperature of 95℃, with rapid stirring. This procedure ensures that during the early stages of the linking reaction, TMS-PDTA/SiO_2 contacts occur preferentially, which favors the linking reaction to silica over the competing polymerization reaction of the TMS-PDTA molecules. After addition of each aliquot, the reaction was allowed to proceed in an open vessel with gentle stirring, until the volume of liquid reduced by half; evaporation of water is required to convert the hydrogen bonds created upon first contact of TMS-PDTA and aqueous SiO_2, to more stable covalent siloxane bridges.

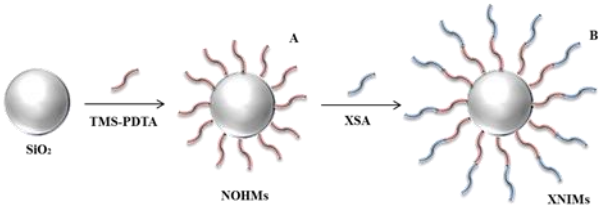

Figure 1. Schematic representation of (A) NOHMs and (B) XNIMs synthesis.

After completion of the linking reaction, unlinked TMS-PDTA and other impurities were removed using a two-step procedure. In the first step, repeated dialysis of the suspension in 10,000 MWCO-snakeskin^{TM} dialysis tubing was performed to remove molecular TMS-PDTA and NaOH. The resultant suspension from step 1 was purified

further by repeated precipitation in tetrahydrofuran (THF, Sigma-Aldrich). This procedure simultaneously removes the inevitable small fraction of TMS-PDTA polymers created in the linking step with M_w greater than the 10,000 MWCO of the dialysis membrane and provides a convenient method for gently (relative to evaporation) stripping the last residue of water from the suspension (water is miscible in all proportions with THF).

To create hybrid lubricants, Synfluid® PAO 100 cSt was obtained from Chevron Phillips Chemical co. and used as received. A solution blending procedure, wherein a 5/1 mixture of toluene and 2-propanol as solvent, was employed to produced PAO-NOHMs composites (as shown in Fig. 2A). Specifically, NOHMs obtained using the procedures outlined in the previous section were first dispersed in the toluene/2-propanol solvent to form a homogeneous, transparent solution. The desired amount of PAO, based on the NOHMs loading targeted, was dissolved in toluene and the solution was added to the NOHMs suspension with vigorous stirring. The resultant composite solution was transferred to a convection oven and the solvent driven off.

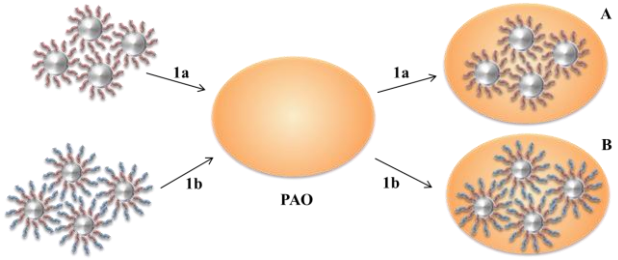

Figure 2. Schematic representation of (A) PAO-NOHMs (path 1a using 5:1 toluene/2-propanol as a solvent) and (B) PAO-XNIMs (path 1b using toluene as a solvent) blending.

TMS-PDTA was selected for this study for at least three reasons. First, it is an amphiphilic molecule that forms stable solutions in water at high PH, as well as in alcoholic solutions of many organic liquids. Second, the large number of accessible amino groups it imparts to the particle surface provides a mechanism for creating

strong, stable bonds with metallic substrates[30]. Even at elevated temperature. Additionally, these tethered amino groups provide numerous sites for additional surface functionalization, which can be used to manipulate dispersion state and interfacial properties of the resulting NOHMs in a range of lubricant base oils. Finally, the material is available inexpensively from multiple commercial sources, which makes it a good candidate for large-scale synthesis of hybrid lubricants. The amphiphilic nature of TMS-PDTA is important because it allows the organosilane linking reaction to be performed on particles in base-stabilized aqueous or alcoholic suspensions; i.e. the native state for most sol-gel derived metal oxide nanostructures. This limits inevitable aggregation that occurs in conventional surface functionalization reactions on nanoparticles, which typically require that the particles are first dried and subsequently re-dispersed in organic solvents such as toluene. A direct benefit is that very high surface coverages ($\sum$ = 1~2 molecules/nm^2), of the silane is achieved; which in turn improves the colloidal stability and tenability of the functionalized nanoparticles.

2.2.b. Preparation of PAO-NIMs composite lubricants

Nanoscale ionic materials (NIMs) were synthesized by tethering base-stabilized, sulfonate-terminated alkylaryl chains to the amine functionalized particles synthesized in II.a. Xylene Sulfonic Acid (XSA-1416, Mw = 396.6 g/mol) was obtained from Oil Chem Technologies, LLC. and used to create an ionically tethered corona around the NOHMs particles (see Fig. 1 (B)). An ion-exchange procedure was used to remove Na^+ ions present in XSA. Specifically Dowex® HCR-W2 (Sigma-Aldrich) ion exchange resin was used at a resin to XSA at a ratio of 20:1 by weight for this purpose. Repeated washing in a non-aqueous media provides an alternative to the ion exchange method[33]. XSA was diluted in a 5/1 mixture of toluene and 2-propanol and the solution run through the ion exchange column 4 times to ensure complete replacement of Na^+ ions with protons, which was confirmed by pH measurements on aqueous solutions of the sulfonic acid form of XSA obtained using the ion exchange procedure.

TMS-PDTA offers optimally 3 amine sites per bound ligand that can be used to form sulfonic acid-amine bonds to tether the XSA chains. To maximize the coverage of XSA, excess XSA was used for the linking step and the excess removed by repeated precipitation. Specifically, NOHMs synthesized in II.a was diluted in a 5/1 mixture of toluene and 2-propanol and stirred overnight to produce a transparent solution. Excess XSA in same solvent mixture was subsequently added and the mixture stirred for 2 days to ensure that the sulfonic-acid amine reaction goes to completion. Solvent from the resulting solution was evaporated in a convection oven for a day, and untethered XSA chains subsequently removed by repeated precipitation using a toluene/methyl alcohol mixed solvent with incremental addition of methyl alcohol for each successive wash. After drying, the resultant soft particles were characterized by thermal gravimetric analysis and the grafting density $\sum$ estimated from the organic content to be 2~3 molecules/nm^2. Unlike their amine-functionalized SiO_2 particle precursors, XSA-NIMs (XNIMs, for simplicity in the following discussion), created using this procedure showed exceptional dispersion in Toluene, consistent with the greater hydrophobicity of the corona imparted by the densely grafted XSA. XNIMs/PAO hybrid luricants (Fig. 2B) were prepared using the same method as employed for the PAO/NOHMs hybrids, except Toluene was used exclusively as the dispersing medium.

2.2.c. NOHMs/NIMs characterization

A Zetasizer Nano ZS (Malvern Instuments Ltd.) was used to measure the hydrodynamic diameter of NOHMs and XNIMs particles. A FEI T12 Spirit TEM STEM was used to obtain transmission electron microscopic (TEM) micrographs of the materials to directly characterize the dispersion state of both types of hybrid nanoparticles in PAO. A Thermo Scientific Inc.'s Thermal gravimetric Analyzer (TGA) was used to quantify the inorganic content in the NOHMs and XNIMs, which allows the respective grafting density to be estimated.

2.2.d. Dynamic mechanical properties of PAO-NOHMs and PAO-XNIMs composite lubricants

Mechanical properties of PAO base oils, PAO-NOHMs and PAO-XNIMs composite lubricants were characterized in a dynamic shear configuration. Specifically, PAO-NOHMs and PAO-XNIMs composites were sandwiched between cone-and-plate fixtures in a mechanical rheometer (MCR 501, Anton Paar Inc.). The MCR was operated in shear mode and reports the elastic/storage modulus, G', and loss modulus, G'', as a function of a variety of variables – shear strain, γ, oscillation frequency, ω, and temperature, T. Moduli measurements at fixed oscillation frequency, temperature, but variable shear strain are particularly useful in that they can be used to quickly establish the universal class (e.g. linearly elastic, non-linear viscoelastic, simple liquid, soft glass, gel) to which our composites belong.

2.2.e. Tribological properties of PAO-NOHMs and PAO-XNIMs composite lubricants.

A ball-on-three-plates tribometer[31] was used for characterizing the interfacial friction behavior of the composite lubricants. Equivalent concentration of PAO-NOHMs and PAO-XNIMs composite lubricants dissolved in solvent was applied on the steel plates and dried completely in convection oven for the testing. These measurements were also performed using the MCR 501 – in this case outfitted with the ball-on-three-plates configuration depicted in Fig. 3. To characterize the tribological behavior of a material, torque and normal force were applied to the shaft and the steel ball rotates relative to the stationary plates. Significantly, the plates sit on a gimbal mount that allows their positions to be adjusted in all directions for even distribution of friction contacts.

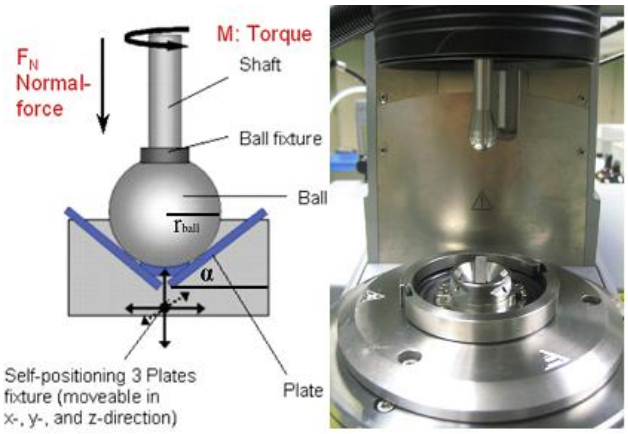

Figure 3. Schematic setup[32] and photograph of the ball-on-three-plates tribometer used for the study.

Additionally, in our experiments the three plates were maintained at an angle $\alpha = 45^{\circ}$ with respect to the measuring cell (Fig. 3) and a steel ball with radius of 6.35 mm was used to induce contacts. Based on this geometrical setup, the normal load and friction force can be calculated as followed:

$$F_L = 2 \cdot F_N \cdot \cos(\alpha) \qquad \text{(eq. 1)}$$

$$F_F = M / (r_{ball} \cdot \sin(\alpha)) \qquad \text{(eq. 2)}$$

$$\mu = F_F / F_L \qquad \text{(eq. 3)}$$

F_N and F_L are the normal force applied and normal load, respectively, M is the torque applied and μ is the friction coefficient. In this study, normal loads of 20 and 60 N were chosen and Stribeck curves were constructed to study the effect of sliding (rotation) speed on the friction coefficient, and investigate the lubrication characteristics of the PAO-NOHMs and PAO-XNIMs composite lubricants in various lubrication regimes.

2.2.f. Thermal stability of PAO-NOHMs and PAO-XNIMs composite lubricants

Temperature-dependent rheology measurements were performed using the MCR 501 to evaluate the thermal stability of the materials. Specifically, cone-and-plate shear

flow was used to measure the shear-rate dependent viscosity, or flow curve, of the materials at two temperatures, 30˚C and 100˚C. Three discrete compositions of NOHMs (4.1, 29, and 45 wt %) and XNIMs (5.5, 38.7, and 60 wt %) in PAO were used for these experiments where each composition is equivalent to SiO_2 contents of 3.7, 26.1, and 40.4 wt%, respectively. The viscosities of many PAO-based lubricating oils are known to decrease markedly with increasing temperature, but even small amounts of nanoparticle additives in the base oil have been reported to dramatically improve thermal stability of their viscous properties[7]. We anticipate that this stabilizing effect of nanoparticles will be as large at the high end of the particle composition range studied.

2.3. Results and Discussion

2.3.a. NOHMs and XNIMs characterization

Fig. 4 reports the size distribution of NOHMs and XNIMs particles measured using a Zetasizer. According to Sigma-Aldrich, the SiO_2 nanoparticles in LUDOX® HS-40 have an average diameter of 12 nm. Fig. 4A shows that the average size of SiO_2 nanoparticles increases after grafting TMS-PDTA. Specifically, the figure shows that the average diameter of the original SiO_2 nanoparticles in deionized water increases from ~12 nm to 31 nm (Fig. 4A). The three-fold increase in diameter is substantially larger than expected from grafting of TMS-PDTA to the original SiO_2 nanospheres. It is tempting to attribute this result to aggregation of the primary NOHMs structures, however the clear narrow particle size distribution achieved with surface functionalization is inconsistent with this explanation. However, when NOHMs are placed in high pH environment where SiO_2 nanoparticles in LUDOX® HS-40 comes as base-stabilized colloidal system to prevent SiO_2 nanoparticles from aggregating, we see that the size distribution of NOHMs becomes consistent with the reported size of SiO_2 nanoparticles. Additionally, we will show later that when these particles are dispersed in hydrophobic PAO and imaged by transmission electron microscopy (TEM), their sizes are substantially smaller and close to that expected for the TMS-

PDTA grafted SiO_2 particles. We therefore conclude that the factor of three enhancements in the average particle diameter seen in Fig. 4A originates from spontaneous, reversible, organization of the amphiphilic particles in pH neutral water. XNIMs particles were prepared in nonpolar solvent, Toluene. Fig. 4B shows clear narrow particle size distribution around the reported size of SiO_2 nanoparticles. This result implies high canopy density of XSA around NOHMs which allows high dispersion in nonpolar medium. We will further show inorganic content measurement from Thermogravimetric Analysis (TGA) which allows canopy grafting density calculation and show TEM image of highly dispersed XNIMs in hydrophobic PAO.

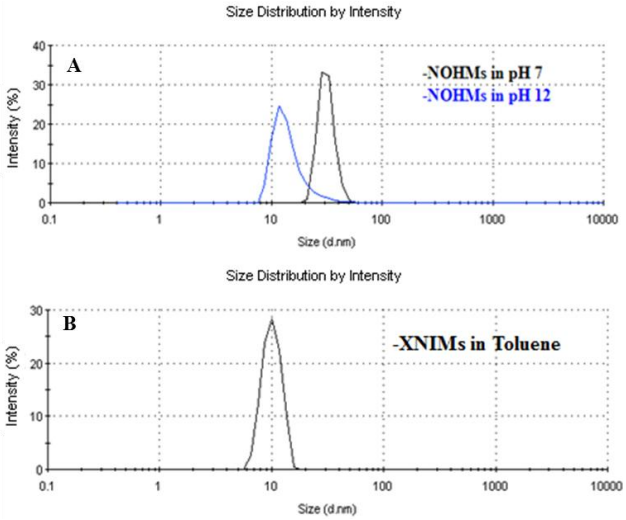

Figure 4. Size distribution of (A) NOHMs in deionized water in pH of 7 and 12 and (B) XNIMs in toluene

Thermal gravimetric analysis (TGA) provides a simple method for quantifying the organic content of any organic-inorganic hybrid material. Fig. 5 shows the thermal degradation of the organic component in PAO, NOHMs, and XNIMs. Temperature was raised from 30°C to 800°C. At this point, only SiO_2, which has a melting temperature of 1650°C at 1 atm, would remain. PAO shows complete degradation at around 500°C as expected. If one assumes that each SiO_2 core particle has, statistically, the same number of reactive surface hydroxyl groups in water, it is straightforward to estimate the number of TMA-PDTA molecules grafted per NOHMs particle. If one

further assumes that the particle surface is well-defined and non-porous, the surface coverage or graft density of TMA-PDTA is determined to be 1.74 molecules/nm^2 of the SiO_2 surface. With same assumption, one can determine XNIMs graft density to be 2.47 molecules/nm^2 of the SiO_2 surface which means that effective ionic tethering ratio is approximately 1.4 XSA chains/TMA-PDTA chain. Since each TMA-PDTA molecule possesses 3 terminal amine groups (one 1^o and two 2^o amines), the ratio of 1.42 XSA chains/TMA-PDTA chain is plausible and other ligand chemistries can be expected to be introduced via the amino groups to enhance compatibility of the hybrids with base oils other than PAO.

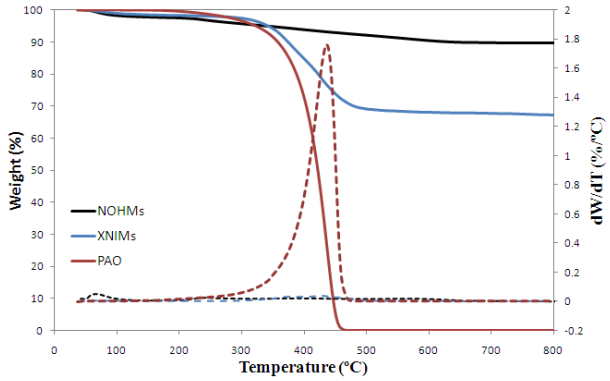

Figure 5. Thermogravimetric Analysis (TGA) of PAO, NOHMs, and XNIMs

We show in Fig. 6A bulk samples of PAO, NOHMs, and PAO-NOHMs composite containing 4.1, 29, and 45 wt% of NOHMs respectively. It can be seen here that clear transparency of PAO is retained even when white powdered form of NOHMs is dispersed in PAO. These results attest to the homogeneous and complete dispersion of the particles into PAO at all compositions studied. This point is confirmed by TEM micrographs (Fig. 7A and 7B) at two magnifications for PAO-NOHMs composite with the highest NOHMs. The TEM images confirm that the hybrid particles exist as primary, un-aggregated nanostructures in the PAO host. As discussed in the introduction, the exceptionally high level of dispersion achieved at these high particle loadings is anticipated to yield many benefits for interfacial friction and wear properties. Indeed in typical base-oil/nanoparticle composites comparable levels of

dispersion are only possible for systems containing 1~3 wt% of nanoparticles and even then significant quantities of dispersant (reaching up to 100 times the weight of nanoparticles) must be added. Flip experiment of PAO-NOHMs composite (shown in Fig. 4C) manifests that depending on amount of NOHMs loading, simple liquids to complex gels can be facilely created. Since mere physical blending of NOHMs nanoparticles endows this property, these types of materials should attract broad-based practical interest.

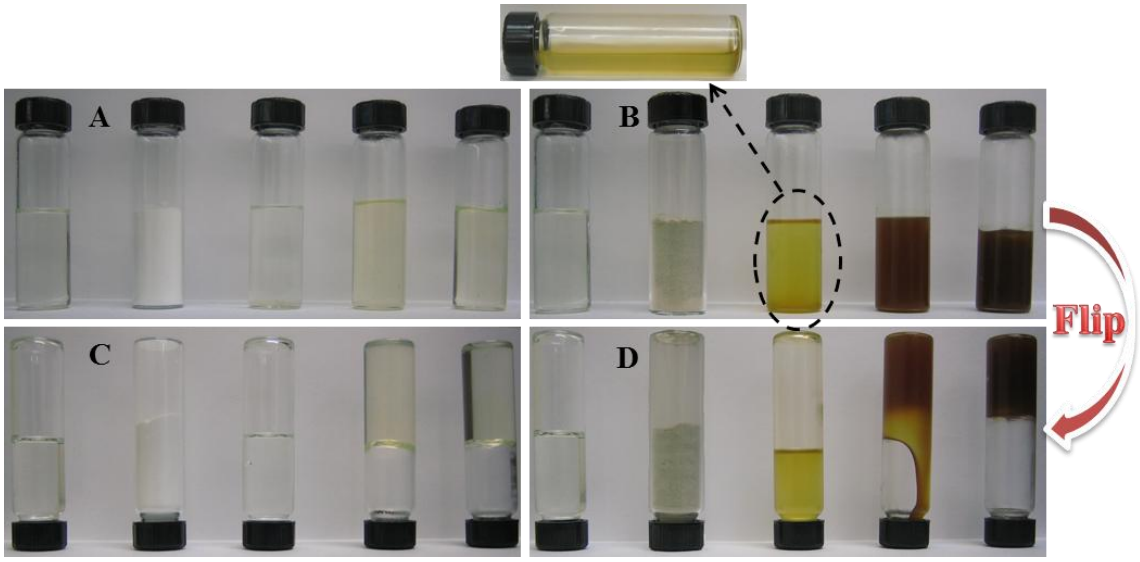

Figure 6. Photograph of (A and C): PAO, NOHMs, and PAO-NOHMs (4.1, 29, 45 wt% NOHMs); and Photograph of (B and D): PAO, XNIMs, PAO-XNIMs (5.5, 38.7, 60 wt% XNIMs). Each PAO based hybrid composites match SiO_2 contents (3.7, 26.1, 40.4 wt% respectively). PAO based hybrid composites shown in A and B were flipped (shown in C and D respectively) and photographed after two days. The horizontal vial on top is included to demonstrate that the brown rings observable at the top and bottom of the upright version of the same vial are entirely a result of lighting effects.

PAO-XNIMs composite samples having similar SiO_2 content as the PAO-NOHMs materials were prepared (Fig. 6B). Due to high grafting density of XSA ($\sum$ = 2.47 molecules/nm^2), XNIMs naturally exist as soft-solids. Additionally, unlike the PAO-NOHMs composites, where good transparency is retained at all particle loadings, at progressively high loadings of XNIMs in PAO the solution color changes from light

yellow to dark brown. This behavior likely originates from the fact that XSA and the resultant XNIMs are brownish in color; it does not arise from agglomeration. This point is again confirmed using TEM of the hybrid lubricants at two magnifications (see Fig. 7C and 7D) for the PAO-XNIMs composite with the highest SiO_2 particle loading. In particular, the TEM images show that the hybrid particles are free of aggregation in the PAO host. Flip experiment was also done with PAO-XNIMs composite (shown in Fig. 6D). PAO-XNIMs composite also suggest that depending on amount of XNIMs loading, simple liquids to complex gels can be facilely created. However, PAO-XNIMs composite endow another striking feature that has not been seen from PAO-NOHMs composite. As can be seen from Fig. 6D, PAO-XNIMs composite with 38.7 wt% XNIMs shows more fluidic character than PAO-NOHMs composite with 29 wt% NOHMs even at approximately 10 wt% more particle loadings in PAO host. This can be explained by chemical compatibility of XSA and PAO. R. Rodriguez et al.[27] have reported that unlike a colloidal suspension where the suspending medium and the particles are physically distinct entities, each particle in a NIMs fluid carries around its share of the suspending solvent. With that being stated, we have discovered that PAO-XNIMs composite with 5.5 wt% XNIMs are in fact viscoelastic gels which we will further discuss it on rheology section.

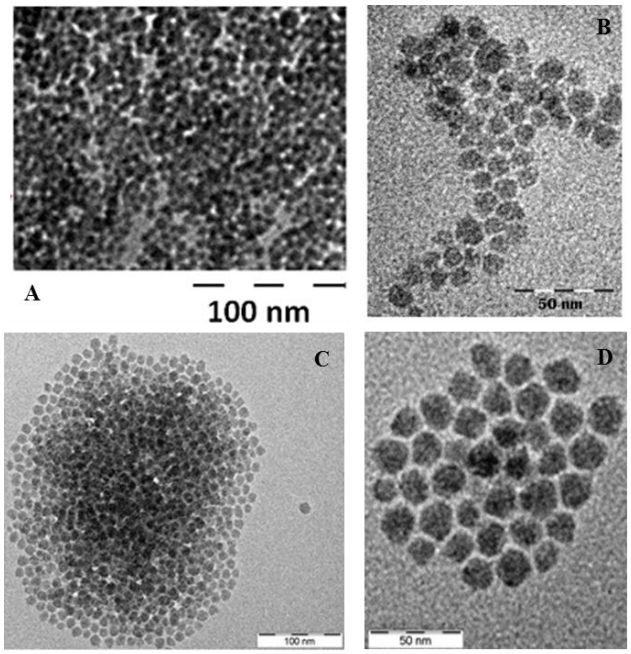

Figure 7. TEM micrograph of PAO-NOHMs composite containing 45 wt% of NOHMs (A and B) and of PAO-XNIMs composite containing 60 wt% of XNIMs (C and D) where A and C are prepared in lower magnification and B and D are prepared in higher magnification.

2.3.b. Rheological characterization of PAO-NOHMs and PAO-XNIMs composite lubricants.

Closer examination of TEM micrograph in Fig.7 indicates that the NOHMs and XNIMs particles are in an extremely crowded environment when dispersed in PAO. This means that motion of any individual particle requires coordinated movements of its neighbors. Thus each SiO_2 core can be thought of as being encaged by surrounding particles; physics that have very recently been shown[26] should lead to soft glassy rheology. As pointed by Agarwal, et al., oscillatory shear rheology measurements, performed at fixed frequency and variable shear strain, provide a straightforward approach for ascertaining whether a material belongs to the *soft-glassy solid* universal class.

Oscillatory shear measurements were performed at a constant angular frequency (ω) = 10 rad/s and at shear strains ranging from 0.01% to 100%. The strain-dependent storage- (G') and loss (G'') moduli deduced from these measurements are reported in Fig. 8A for PAO-NOHMs composites with varying NOHMs content and Fig.8B for PAO-XNIMs composites with varying XNIMs content. It is apparent from the figure that at low shear strains, both moduli are independent of shear strain for all materials studied; this range of strain defines the so-called linear viscoelastic LVE shear regime[33]. It is also apparent that, with the exception of PAO, all materials manifest non-negligible storage and loss moduli, an indication that the composites are viscoelastic materials. For PAO, the loss (viscous) modulus is small, but still dominates the storage modulus $G'' > G'$ over the entire range of shear strains studied. This means that without any further treatment, PAO itself can be thought of as an ideal-viscous liquid.

As NOHMs nanoparticles are incorporated into PAO at progressively higher loadings, the material shows several transitions - from viscoelastic liquid to viscoelastic gels, notably without losing its homogeneity (Fig. 6A). In particular the PAO-NOHMs composite with 4.1 wt% NOHMs nanoparticles show a small amount of elasticity, but G'' is substantially unchanged from that of the base PAO liquid and remains larger than G' at all shear strains; indicative of viscoelastic liquid behavior. When the NOHMs composition is increased to 29 wt%, completely different behavior is observed. Not only is the elastic modulus now dominant ($G' > G''$) at strains in the LVE regime, but it is more than 4 orders of magnitude greater than G' for PAO. Additionally, at small shear strains G'' is substantially higher than for PAO. Together, these results mean that the material is both substantially stronger and much thicker (more viscous) than PAO; both effects are significantly enhanced when the NOHMs content is increased to 45 wt%. If one ignores the strain dependence of the moduli, our observations would imply that the latter two PAO-NOHMs composites are viscoelastic gels. The strain dependence of both moduli is, however, significant and cannot be ignored. In fact both materials exhibit transitions from G'-dominant

(solid-like) to G′′-dominant (liquid-like) behavior at shear strains 6.4% and 10.7%, respectively. As shown in Fig. 9A, the shear stress manifests a visible change of slope at strains coincident with the observed transition from solid-like to liquid-like behavior. This type of behavior is characteristic of a yielding transition and is not seen in PAO or in the PAO-NOHMs composite with 4.1 wt% NOHMs. It is strikingly similar to the transition reported by Agarwal et al., for their self-suspended nanopaticle suspensions, which suggests that the PAO-NOHMs composites with 29 and 45 wt% NOHMs are in reality soft glasses.

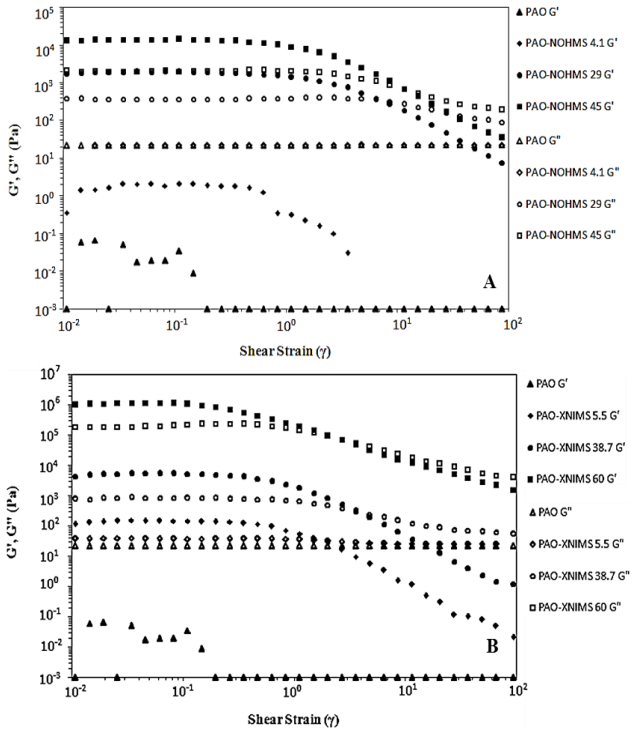

Figure 8. Shear modulus versus strain of: A. PAO-NOHMs composites (0, 4.1, 29, 45 wt%) and B. PAO-XNIMs composites (0, 5.5, 38.7, 60 wt%)

The same analysis was performed on the PAO-XNIMs composite to study their rheological behavior. At each XNIMs loading, G′ was found to be approximately an order of magnitude greater than the corresponding value for PAO-NOHMs composites at a comparable SiO_2 particle loading. These changes lead to subtle, but important

differences between the two types of composites. For example, the vial inversion experiment (Fig. 6D) for a PAO-XNIMs containing 5.5 wt% XNIMs shows decidedly fluid-like behavior, however the more detailed insight made possible by the rheological measurements (Fig. 8B and Fig. 9B), clearly show that the materials are in reality viscoelastic gel. An even more profound example of the same behavior is manifested by the PAO-XNIMs with 38.7 wt% XNIMs nanoparticles. This material contains approximately 10 wt% more particles than PAO-NOHMs with 29 wt% NOHMs. Consistent with this difference in composition, the vial inversion experiment in Fig. 6 shows that it is more fluid-like, yet the more detailed rheology measurements shows that the PAO-XNIMs composite is significantly more elastic. In summary, rheological measurements PAO-XNIMs are viscoelastic materials and that they manifest soft *glassy* characteristics at particle loadings well-below where this behavior is seen in PAO-NOHMs. We tentatively attribute this feature to jamming between the longer corona chains in the PAO-XNIMs; its effect on tribomechanical properties is considered next.

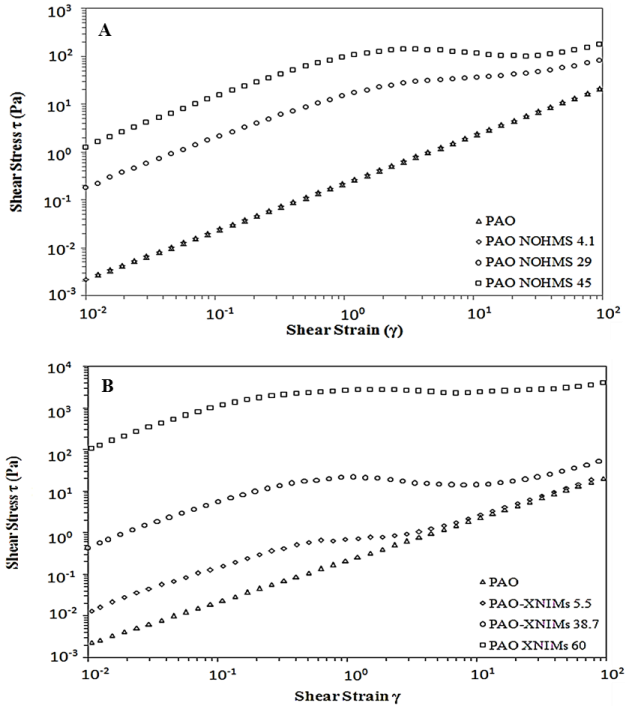

Figure 9. Shear stress versus strain of: A. PAO-NOHMs composites (0, 4.1, 29, 45 wt%) and B. PAO-XNIMs composites (0, 5.5, 38.7, 60 wt%)

2.3.c. Tribology Analysis of PAO-NOHMs and PAO-XNIMs composite lubricants.

The Stribeck Curve (Fig.10) is widely viewed as an extremely useful construction for determining conditions where a material functions as a boundary-, mixed-, elastohydrodynamic- (EHL), or hydrodynamic lubricant[34-38]. This designation is important because each lubrication regime represents distinct characteristic of the contacting surfaces. The Boundary lubrication regime typically occurs at very low speeds where load is carried by asperity points. The lubricant film is very thin in this case thus no pressure is built up. The Mixed lubrication regime also occurs at low speeds, but the load carried by a combination of contact pressure and hydrodynamic pressure in the lubricant film. A thin lubricant film is typically formed in this regime and the hydrodynamic pressure contribution to the load carrying capacity is relatively small. The Elastohydrodynamic lubrication regime occurs at intermediate speeds and a thin lubricant film carries an increasing portion of the load, relative to the load borne by contact points. Here, hydrodynamic pressure is larger and increases gradually with sliding speed. The Hydrodynamic lubrication regime occurs at high speeds and the contact points are completely separated by the lubricant film. Hydrodynamic pressure and load come into equilibrium and the thickness of the lubricant film increases as speed increases.

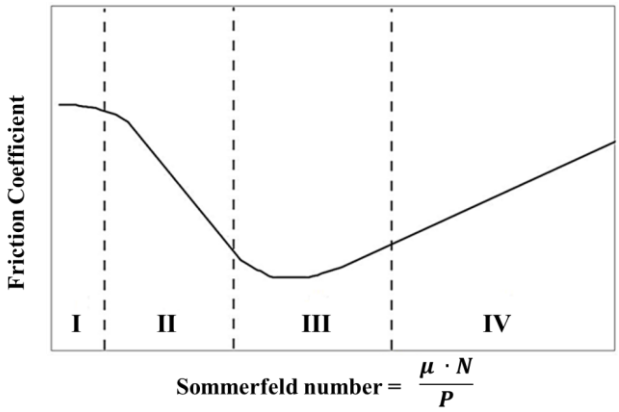

Figure 10. Stribeck curve and regimes of lubrication: I. Boundary; II. Mixed; III. EHL; and IV.Hydrodynamic (μ: kinematic viscosity, N: rotation speed, P: normal load).

The ball-on-three-plates apparatus depicted in Fig. 3 was used to characterize the friction coefficient of PAO, PAO-NOHMs composites, and PAO-XNIMs composite. Sommerfeld number,

$$\text{Sommerfeld number} = (\mu \cdot N) / P \qquad \text{(eq. 4)}$$

was used to construct the Stribeck curve for these materials. Here μ is the kinematic viscosity; N the rotation speed; and P the normal load. This form of modified Sommerfeld number is widely used to characterize construct Stribeck curve and it has a unit of distance over mass (meter/kg in our case). As shown in Fig. 11A, when blank PAO and PAO with 4.1 wt% NOHMs loading were used, typical Stribeck curve behavior is observed, in which the friction coefficient first reaches a minimum in the EHL regime, which is followed by a rapid increase at high speeds; reflecting a buildup of hydrodynamic pressure. It is apparent from the figure that PAO with 4.1 wt% NOHMs loading displays moderately improved friction properties relative to pure PAO. Specifically, the PAO-NOHMs composite manifests a minimum friction coefficient of 0.073 under 20N and 0.076 under 60N, which are measurably lower than the corresponding values for PAO, 0.1 at 20N and 0.09 at 60N. In addition, the EHL regime for the PAO/NOHMs composite is elongated by a factor close to 2. By equation (4), the Sommerfeld number is proportional to shaft rotation speed, indicating that the composite containing 4.1 wt% NOHMs provides better lubrication at more than twice the rotation speed. In the case of the PAO-NOHMs composite containing 29 wt% NOHMs, the minimum friction coefficient achieved is 0.09 at 20N, which is a 10% reduction relative to the untreated PAO. However under a normal load of 60N (Fig.12A), a higher minimum friction coefficient of 0.1, i.e. 11% higher than the unmodified PAO, is observed. Remarkably, we find however that at both loads the breadth of the EHL regime of the PAO-NOHMs composite increases by more than

one order of magnitude. The enhancements in the EHL regime are seen to be even larger for the PAO-NOHMs composite containing 45 wt% NOHMs.

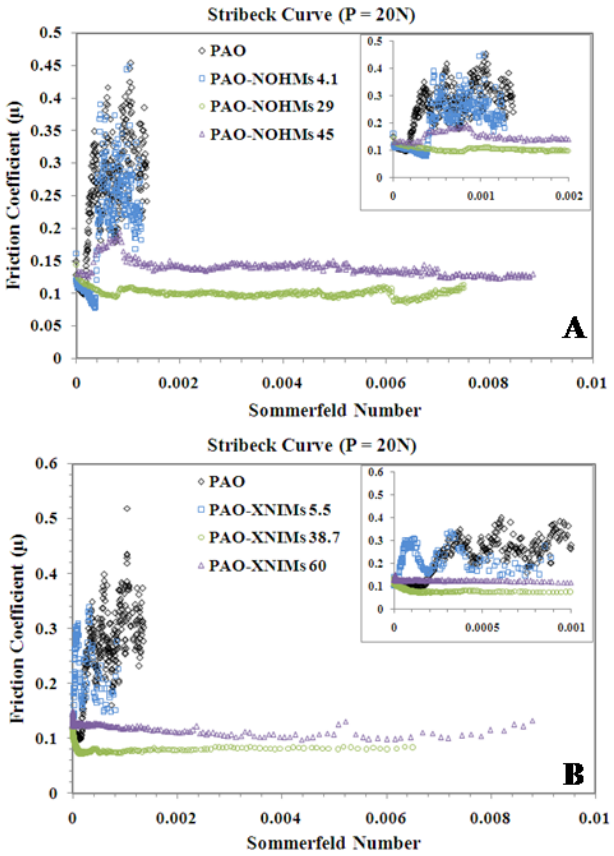

Figure 11. Stribeck curve of: A. PAO-NOHMs composites (0, 4.1, 29, 45 wt%) and B. PAO-XNIMs composites (0, 5.5, 38.7, 60 wt%) both under normal load of 20N at 30 ℃. An amplified view of lower Sommerfeld number regime is provided in the inset.

More careful analysis of the Stribeck curves for the PAO-NOHMs composites with 29 and 45 wt% NOHMs indicate that the EHL regime in these materials is more complex than typically seen in lubricants. Both materials show a regime of increasing friction coefficient at Sommerfeld numbers comparable to where the EHL ends in PAO with low NOHMs loadings. Surprisingly, this regime ends before the hydrodynamic regime is achieved and the friction coefficient falls back to values close to the minima at the onset of the EHL. This behavior appears unique to the PAO/NOHMs composite

lubricants and we believe is responsible for the dramatic extensions in the EHL achieved. We believe that the initial rise in the friction coefficient at intermediate Sommerfeld numbers originates from the jamming of the NOHMs particles already hypothesized from the earlier rheology experiments. Once the cages constraining the structures are broken down by deformation, the material yields and the measured friction reflects the lubrication of PAO chains trapped between NOHMs particles in the composites.

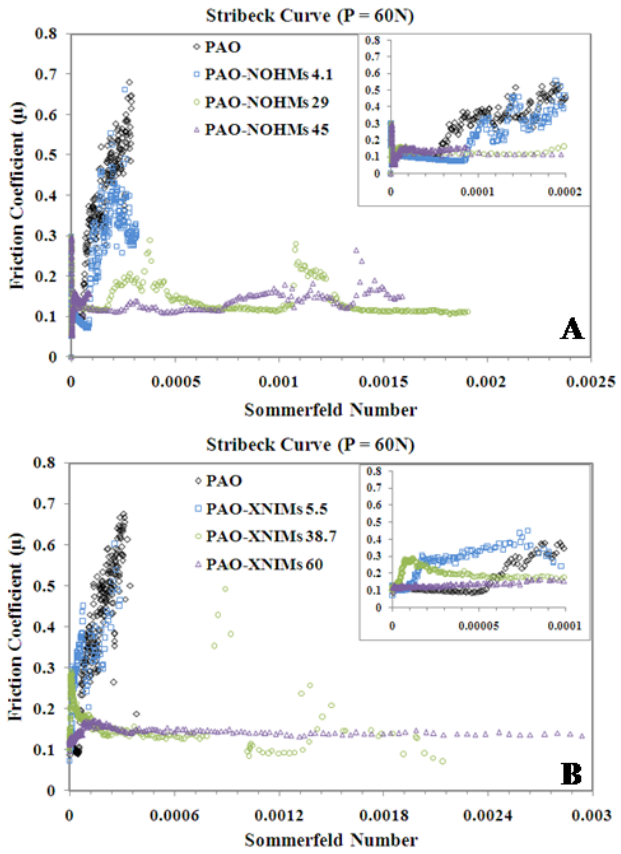

Figure 12. Stribeck curve of: A. PAO-NOHMs composites (0, 4.1, 29, 45 wt%) and B. PAO-XNIMs composites (0, 5.5, 38.7, 60 wt%) both under normal load of 60N at 30 ℃. Close-up view of lower Sommerfeld number regime is offered in the inset.

As shown in Fig. 11B and Fig. 12B, PAO-XNIMs composite with 5.5 wt% of XNIMs loading exhibits typical Stribeck curve behavior under both 20N and 60N of normal

load. However, neither improved friction properties nor EHL regime elongation was observed. On the contrary, PAO-XNIMs composite containing 38.7 wt% XNIMs showed minimum friction coefficient of 0.07 at 20N, which is approximately 38.6% reduction relative to the untreated PAO. We also observed remarkably increased breadth of the EHL regime yet with no sign of jamming effect which was seen from PAO-NOHMs composite systems which further confirm our finding that PAO-XNIMs composite offers higher level of dispersion in PAO. PAO-XNIMs composite containing 60 wt% XNIMs did not improve magnitude of minimum friction coefficient, but exhibited same benefits offered from PAO-XNIMs composite containing 38.7 wt% XNIMs. However as with PAO-NOHMs composite, higher minimum friction coefficients were obtained under a normal load of 60N for both PAO-XNIMs composite containing 38.7 and 60 wt% XNIMs. Jamming effect was also observed under normal load of 60N but as shown in Fig. 12B, its impact is significantly minimized.

The anti-wear and friction-reduction properties of the PAO-NOHMs and PAO-XNIMs composites were evaluated further by increasing the shaft rotation speed to 500 rpm and holding this speed for 10 minutes under normal loads of 20N and 60N at 30˚C. This speed corresponds to lubrication regime where blank PAO, PAO-NOHMs with 4.1 wt% NOHMs loading, and PAO-XNIMs with 5.5 wt% XNIMs loading are well into the hydrodynamic lubrication regime and PAO-NOHMs with 29 and 45 wt% NOHMs loading and PAO-XNIMs with 38.7 and 60 wt% XNIMs loading are in the mixed and EHL regime. Because the PAO-NOHMs composites with 29 and 45 wt% NOHMs loading and PAO-XNIMs with 38.7 and 60 wt% XNIMs loading have lower friction coefficient at these high Sommerfeld numbers, they are anticipated to have better wear reduction characteristics than PAO. The surface morphology of the wear track, roughness of the material in the wear track, and the wear volume were obtained using a MicroXAM Surface profiler. The average surface roughness values for steel plates and steel balls used in this experiment are 0.437 and 1.19 μm respectively. After each wear-test, the surface roughness values are shown in Table 1 and it can be seen

that PAO with NOHMs loading and PAO with XNIMs loading more effectively reduces surface roughness than the blank PAO. It is important to point out that for all tests, surface roughness increased approximately tenfold as normal load was increased from 20N to 60N except of PAO with high XNIMs loadings where almost no improvement in surface roughness is obtained.

	R_a under P = 20 N, 30 ˚C (µm)	R_a under P = 60 N, 30 ˚C (µm)	R_a under P = 20 N, 100 ˚C (µm)
PAO	$9.76 \cdot 10^{-1}$	9.47	3.05
PAO-NOHMs 4.1	$5.30 \cdot 10^{-3}$	$9.79 \cdot 10^{-2}$	$8.63 \cdot 10^{-2}$
PAO-NOHMs 29	$8.21 \cdot 10^{-5}$	$1.08 \cdot 10^{-4}$	$4.83 \cdot 10^{-4}$
PAO-NOHMs 45	$1.61 \cdot 10^{-5}$	$1.67 \cdot 10^{-4}$	$2.07 \cdot 10^{-4}$
PAO-XNIMs 5.5	$4.58 \cdot 10^{-2}$	$1.64 \cdot 10^{-2}$	$1.94 \cdot 10^{-2}$
PAO-XNIMs 38.7	$7.10 \cdot 10^{-4}$	$5.43 \cdot 10^{-4}$	$1.20 \cdot 10^{-4}$
PAO-XNIMs 60	$6.11 \cdot 10^{-5}$	$5.62 \cdot 10^{-5}$	$4.22 \cdot 10^{-5}$

Table 1. Surface Roughness (R_a) under load of 20 and 60 N at 30˚C and 20 N at 100 ˚C

Two-dimensional surface profiles under normal load of 20N and 60N are shown in Fig. 13 and 14, respectively. Each surface profiles' XYZ-scale has been taken at the optimal setting to visualize the wear effect. Wear tests with blank PAO shows both the largest wear area and depth except of PAO-XNIMs composite with 5.5 wt% XNIMs

loading. All other NOHMs and XNIMs loadings the PAO-NOHMs and PAO-XNIMs composites display reduced wear area as well as depth. As can be seen from Fig. 13A, a 2mm x 2mm image had to be taken to fully capture the wear surface morphology of steel plates when blank PAO was used, which makes the intact part of steel surface appear smoother. The wear volume reduction is more conspicuous with PAO with 29 and 45 wt% NOHMs loading and PAO with 38.7 and 60 wt% XNIMs loading, for which considerable reductions in the wear track depth and smoothening of the wear area are observed. Comparable wear volume was detected with these materials. Under 20N, PAO with 60 wt% XNIMs yielded the lowest wear volume of all materials studied; and under 60N, PAO with 60 wt% XNIMs once again yielded the largest reduction in wear volume; implying that it is most effective as an anti-wear agent at higher normal loads. All wear volume testing results are offered in table 2.

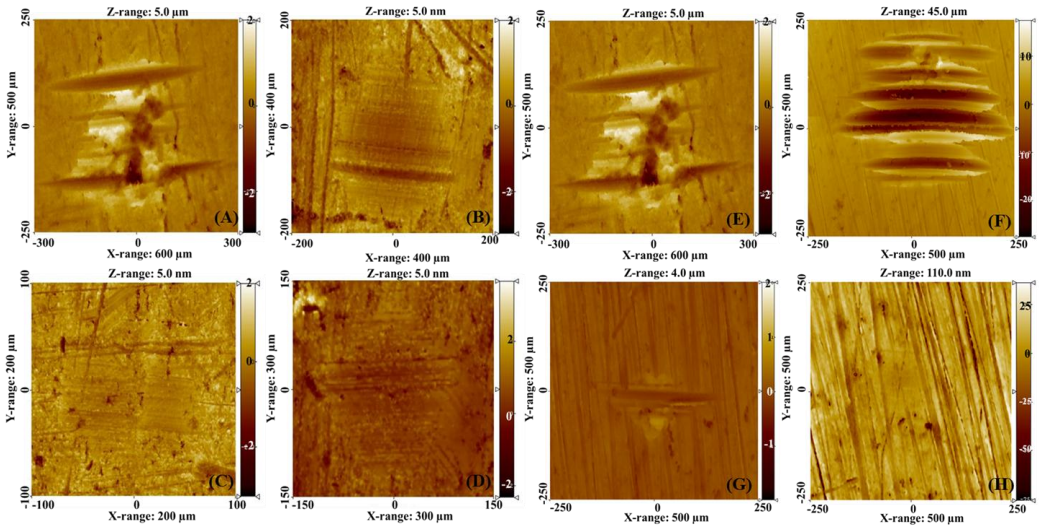

Figure 13. Two-Dimensional surface profiles under normal load of 20N at 500 rpm for 10 minutes at 30˚C (PAO-NOHMs composites with (A) 0, (B) 4.1, (C) 29, (D) 45 wt% NOHMs loading and PAO-XNIMs composites with (E) 0, (F) 5.5, (G) 38.7, (H) 60 wt% XNIMs loading)

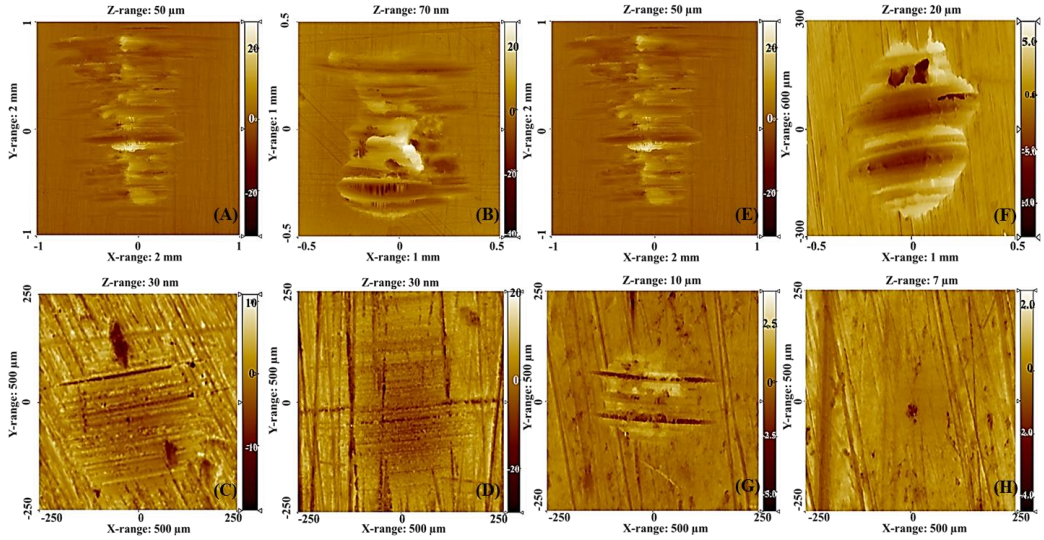

Figure 14. Two-Dimensional surface profiles under normal load of 60N at 500 rpm for 10 minutes at 30˚C (PAO-NOHMs composites with (A) 0, (B) 4.1, (C) 29, (D) 45 wt% NOHMs loading and PAO-XNIMs composites with (E) 0, (F) 5.5, (G) 38.7, (H) 60 wt% XNIMs loading).

	Wear Volume under P = 20 N, 30 ˚C (μm^3)	Wear Volume under P = 60 N, 30 ˚C (μm^3)	Wear Volume under P = 20 N, 100 ˚C (μm^3)
PAO	$5.33 \cdot 10^3$	$1.21 \cdot 10^6$	$1.64 \cdot 10^5$
PAO-NOHMs 4.1	$6.40 \cdot 10^1$	$4.23 \cdot 10^2$	$1.94 \cdot 10^4$
PAO-NOHMs 29	3.46	$3.24 \cdot 10^1$	$6.62 \cdot 10^2$
PAO-NOHMs 45	4.19	$1.86 \cdot 10^1$	$8.19 \cdot 10^1$
PAO-XNIMs 5.5	$4.20 \cdot 10^4$	$2.50 \cdot 10^5$	$4.00 \cdot 10^4$
PAO-XNIMs 38.7	$6.25 \cdot 10^1$	$7.00 \cdot 10^2$	$3.50 \cdot 10^3$
PAO-XNIMs 60	$2.00 \cdot 10^{-1}$	$1.50 \cdot 10^{-1}$	$4.00 \cdot 10^3$

Table 2. Wear volume under load of 20 and 60 N at 30˚C and 20 N at 100 ˚C

The increase in load-carrying capacity of the PAO-NOHMs composites with high NOHMs loadings and PAO-XNIMs composites with high XNIMs loadings can be explained in terms of the nanoparticles filling the wear track, which reduce asperity contacts thus facilitating formation of a boundary lubricating film. The boundary lubricating film is anticipated to be very thin, but its presence is clearly important for imparting anti-wear properties. To evaluate the hypothesis that the anti-wear properties of the PAO-NOHMs composites and PAO-XNIMs composites arise from the ability of the nanostructures to fill the wear track, we characterized the chemistry of the wear track using EDS. The results shown in Fig. 15 are for the PAO-NOHMs composite with 45 wt% NOHMs loading and PAO-XNIMs composite with 60 wt% XNIMs loading after 10 minutes of ultrasonication in chloroform. Elemental analysis appears to confirm our earlier hypothesis that silica particles have effectively filled the surface scars.

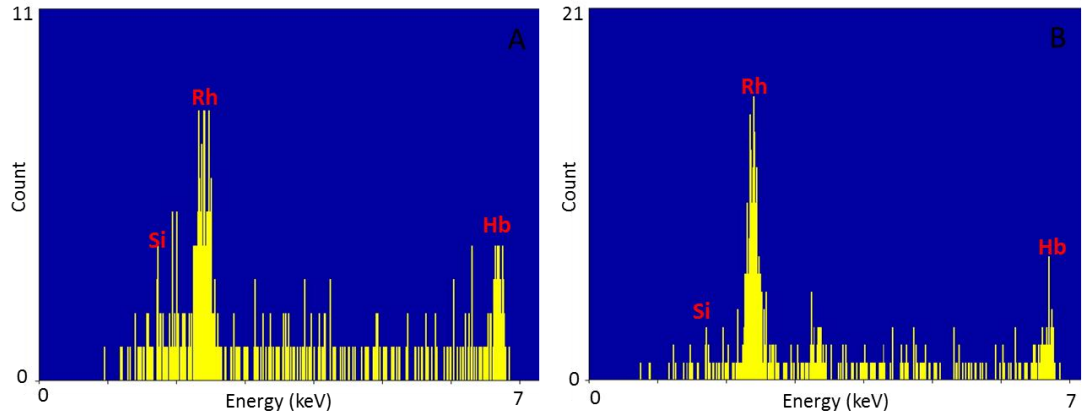

Figure 15. Elemental Analysis of wear track for: A. PAO-NOHMs composite with 45 wt% NOHMs loading and B. PAO-XNIMs composite with 60 wt% NOHMs loading.

Interfacial friction measurements were also performed under normal load of 20N at 100˚C to evaluate the effect of temperature on performance of our PAO-NOHMs and PAO-XNIMs composite lubricants. Fig. 16 is the Stribeck curve obtained from these measurements. Compared to the result obtained under the same normal load, 20N, at 30˚C (Fig.11), a general shortening of the EHL regime can be observed for all materials. It is known that because the viscosity of most lubricants are lower at these high temperatures a good lubricant film between contacting surfaces cannot be easily established[6]. The more trivial reduction in the Sommerfeld number for the lower lubricant viscosity obviously also plays a role[11]. Remarkably, even though the EHL regime is truncated, the PAO-NOHMs composite with 45 wt% NOHMs exhibits a 50% lower minimum friction coefficient than PAO (0.06 versus 0.12) and again displays a substantially enhanced EHL regime. However, PAO-XNIMs composite at 5.5 and 38.7 wt% XNIMs loadings decreased EHL regime yet offered lower minimum coefficients where PAO-XNIMs composite with 38.7 wt% XNIMs loading offered minimum friction coefficient of 0.03. PAO-XNIMs composite with 60 wt% XNIMs loading exhibited both lower minimum coefficient and longer EHL regime than PAO with no particle loadings. We speculate that as PAO-XNIMs are functionalized by

PAO-compatible chains, XNIMs are also subjected to viscosity decrease as temperature is raised. Thus, we suspect that if we can create XSA with higher molecular weight, self-suspending nanocomposite lubricant can be created with better performance.The anti-wear and friction-reduction properties at the higher temperature were evaluated using the same procedure employed at lower temperature. The two-dimensional surface profile shown in Fig. 17, again shows that the presence of the hybrid particles in PAO significantly reduces both the wear track area and depth. Tables 1 and 2 summarize surface roughness (Ra) values and wear volume data deduced from the images in Fig.17. It is evident from the table that while all samples display increased surface roughness and wear volume at the higher temperature, the lowest increases in all characteristics of wear are observed for the PAO-NOHMs composite with 45 wt% NOHMs loading.

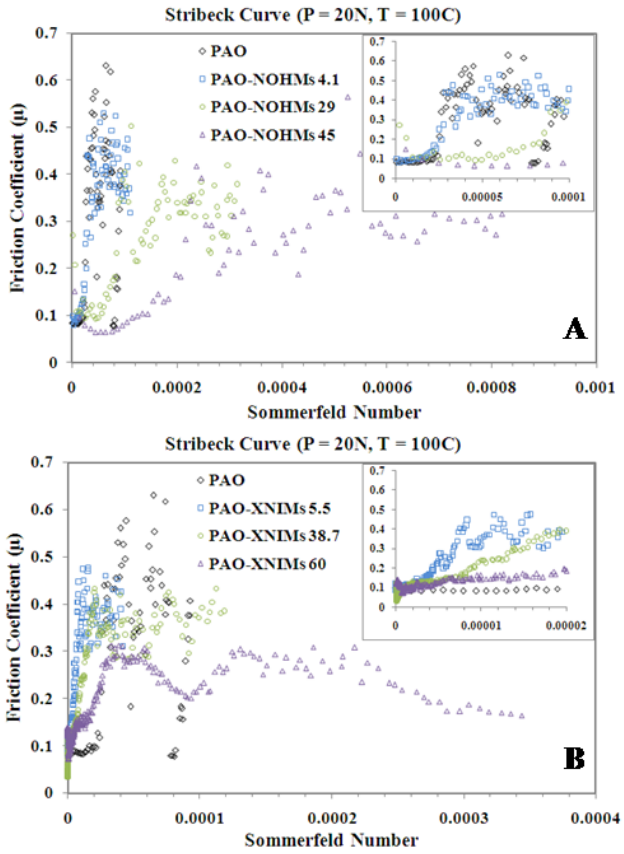

Figure 16. Stribeck curve of: A. PAO-NOHMs composites (0, 4.1, 29, 45 wt%) and B. PAO-XNIMs composites (0, 5.5, 38.7, 60 wt%) both under normal load of 60N at 100 ℃. An expanded view of the lower Sommerfeld number regime is provided in the inset.

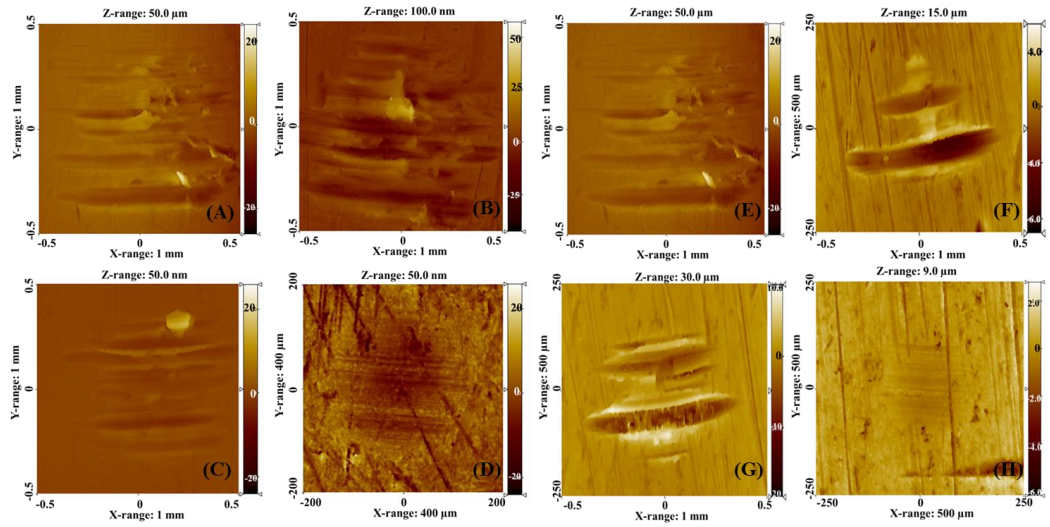

Figure 17. Two-Dimensional surface profiles under normal load of 20N at 500 rpm for 10 minutes at 100˚C (PAO-NOHMs composites with (A) 0, (B) 4.1, (C) 29, (D) 45 wt% NOHMs loading and PAO-XNIMs composites with (E) 0, (F) 5.5, (G) 38.7, (H) 60 wt% XNIMs loading).

2.4. Conclusion

Despite the well-known benefits of adding nanoparticles to base lubricating oils to improve their interfacial friction and wear properties, aggregation and/or phase separation of nanoparticles have prevented these benefits from being realized in practical nanocomposite lubricants. In this study, we report that silica (SiO_2) nanoparticles densely grafted with amphiphilic organic chains can be homogeneously dispersed in polyalphaolefin (PAO) base oils to form stable nanoscale organic-inorganic hybrid lubricants at both low and high particle loadings. A PAO-XNIMs composite with 60 wt% XNIMs has been shown to simultaneously lower the interfacial friction coefficient, enhance wear and mechanical characteristics, and to yield nanocomposite lubricants that exhibit superior stability to PAO or its nanocomposites created at low nanoparticle loadings. Similar effects are also reported for a PAO-NOHMs composite with 45 wt% NOHMs, but in this case the interfacial properties of the composite material also display attractive thermal stability. Physical and Chemical analysis of the wear track using profilometry and energy dispersive x-

ray spectroscopy shows that the anti-wear benefits of the NOHMs and XNIMs stem from their ability to deposit in the wear track and reinforce the interface between approaching solids at high sliding speeds. Thus, we conclude that PAO-NOHMs composite and PAO-XNIMs composite are good systems for delivering enhanced lubrication performance and wear resistance in demanding applications. Finally, judging from the simplicity of the synthesis of the PAO-NOHMs and PAO-XNIMs composite lubricants and the large libraries of nanoparticles, lubricant base oils, tethered polymer chemistries, molecular weights, and architectures that can be employed, we anticipate that this lubricant platform will find broad applicability in formulations of new types of waxes and greases capable of delivering attractive interface stability, without compromising higher tolerances demanded in high-performance machines.

References

(1) Bhushan B.; Israelachvili, J. N.; Landman, U. *Nature*. **1995**, *374,* 607.

(2) Chowdhury, M.A.; MaksudHelali Md. *Wear*. **2007**, *262*, 198.

(3) Demydov, D.; Adhvaryu, A.; McCluskey, P.; Malshe, A. P. *ACS Symposium Series*. **2010**, *1045 (8)*, 137.

(4) Puniredd, S. R.; Wai, Y. K.; Satyanarayana, N.; Sinha, S.; Srinivasan, M. P. *Langmuir*. **2007**, 23, 8299.

(5) Ou, J.; Wang, J.; Liu, S.; Mu, B.; Ren, J.; Wang, H.; Yang. S. *Langmuir*. **2010**, *26(20)*, 15830.

(6) Urbakh, M.; Klafter, J.; Gourdon, D.; Israelachvili, J. *Nature*. **2004**, *430*, 525.

(7) Zhang, M.; Wang, X.; Fu, X.; Xia, Y. *Trib. Int.* **2009**, *42*, 1029.

(8) Battez, A.; Rico, J.E.; Arias, A.; Rodriguez J.L.; Rodriguez R.; Fernandez J.M. *Wear*. **2006**, *261*, 256.

(9) Yu, H.; Xu, Y.; Pei-jing, S.; Xu, B.; Wang, X.; Liu, Q. *Trans. Nonferrous Met. Soc. China*. **2008**, *18*, 636.

(10) Wu, Y. Y.; Tsui, W.C.; Liu, T.C. *Wear*. 2007, *262*, 819.

(11) Qiu, S.; Zhou, Z.; Dong, J.; Chen, G. *J. Trib*. **2001**, *123(3)*, 441

(12) Dong, J. X.; Hu, Z. S. *Trib. Int.* **1998**, *31(5)*, 219.

(13) Liu, W.; Chen, S. *Wear*. **2000**, *238*, 120.

(14) Chen, S.; Liu, W. *Mater. Res. Bull*. **2001**, *36*, 137.

(15) Xue, Q.; Liu, W.; Zhang, Z. *Wear*. **1997**, *213*, 29.

(16) Chen, S.; Liu, W.; Yu, L. *Wear*. **1998**, *218*, 153.

(17) Zhou, J.; Yang J.; Zhang Z.; Liu W.; Xue, Q. *Mater. Res. Bull*. **1999**, *34 (9)*, 1361.

(18) Li, X.; Cao, Z.; Zhang, Z.; Dang, H. *Applied Surface Science*. **2006**, *252*, 7856.

(19) Choi, Y.; Lee, C.; Hwang, Y.; Park, M.; Lee, J.; Choi, C.; Jung, M. *Curr. App. Phys.* **2009**, *9*, 124.

(20) Lee, C.; Hwang, Y.; Choi, Y.; Lee, J.; Choi, C.; Oh, J. *International Journal of Precision Engineering and Manufacturing*. **2009**. *10 (1)*, 85.

(21) Shahar, C.; Zbaida, D.; Rapoport, L.; Cohen, H.; Bendikov, T.; Tannous, J.; Dassenoy, F.; Tenne, R. *Langmuir*. 2010, *26(6)*, 4409.

(22) Rapoport, L.; Lvovsky, M.; Lapsker, I.; Leshchinsky, V.; Volovik, Y.; Feldman, Y.; Margolin, A.; Rosentsveig, R.; Tenne, R. *Nano Lett.* **2001**, *1(3)*, 137.

(23) Nugent, J.L.; Moganty, S.S.; Archer, L.A. *Adv. Mater.* **2010**, *22*, 3677.

(24) Yu, N-Y.; Koch, D.L. *Langmuir* **2010**, 26, 16801

(25) Rodriguez, R.; Herrera, R.; Archer, L.A.; Giannelis, E.P. *Adv. Mater.* **2008**, *20*, 4353.

(26) Argarwal, P.; Qi, H.; Archer, L. A. *Nano Lett.* **2009**, *10*, 111.

(27) Moganty, S.S.; Jayaprakash, N.; Nugent, J.L.; Shen, J.; Archer, L.A. *Angew. Chem.* **2010**, *49*, 9158.

(28) Zhang, Q.; Archer L.A. *Langmuir*. **2007**, *23*, 7562.

(29) Landherr, L. J. T.; Zhang, Q.; Cohen, C.; Archer L.A. *J. Poly. Sci. B, Polym. Phys. Ed.*. **2008**, *46*, 1773.

(30) Herve, A.; Yaouanc, J.; Clement, J.; Abbayes, H. *Journal of Organometallic Chemistry*. **2002**, *664*, 214.

(31) Bodamer, G.; Kunin R. *Ind. Eng. Chem.* **1953**, *45, 11*, 2577.

(32) Lauger, J.; Heyer P. *Adv. Trib*. **2009**, *Part 3 (1)*, 61.

(33) Mezger, T. T*he Rheology Handbook.2nd edition. Hannover: Vincent Network.* **2006**. *8, 126*.

(34) Lu, X.; Khonsari, M. M. *Journal of Tribology*. **2006**, *128, 789*.

(35) Zeng, H.; Tian, Y.; Zhao, B.; Tirrell, M.; Israelachvili, J. *Langmuir*. **2009**, *25*, 1954.

(36) Yakubov, G. E.; McColl, J.; Bongaerts, J. H. H.; Ramsden, J. *Langmuir*. **2009**, *25*, 2313.

(37) Colton, R. J. *Langmuir*. **1996**, *12*, 4574.

(38) Sivan, S.; Schroeder, A.; Verberne, G.; Merkher, Y.; Diminsky, D.; Prieve, A.; Maroudas, A.; Halperin, G.; Nitzan, D.; Etsion, I.; Barenholz, Y. *Langmuir*. **2010**, *26*, 1107.